CRISM multispectral summary products: Parameterizing mineral diversity on Mars from reflectance

S. M. Pelkey,[1] J. F. Mustard,[1] S. Murchie,[2] R. T. Clancy,[3] M. Wolff,[3] M. Smith,[4] R. Milliken,[1] J.-P. Bibring,[5] A. Gendrin,[1] F. Poulet,[5] Y. Langevin,[5] and B. Gondet[5]

Received 20 September 2006; revised 15 November 2006; accepted 15 December 2006; published 18 July 2007.

[1] The Compact Reconnaissance Imaging Spectrometer for Mars (CRISM) aboard the Mars Reconnaissance Orbiter (MRO) is the most recent spectrometer to arrive at Mars. The instrument is a hyperspectral imager covering visible to near-infrared wavelengths (0.37–3.92 μm at 6.55 nm/channel). Summary products based on multispectral parameters will be derived from reflectances in key wavelengths for every CRISM observation. There are 44 summary products formulated to capture spectral features related to both surface mineralogy and atmospheric gases and aerosols. The intent is to use the CRISM summary products as an analysis tool to characterize composition as well as a targeting tool to identify areas of mineralogic interest to observe at higher spectral and spatial resolution. This paper presents the basis for the summary products and examines the validity of the above approach using data from the Mars Express OMEGA instrument, a visible/near-infrared imaging spectrometer with spatial and spectral coverage similar to that of CRISM. Our study shows that the summary products vary in utility, but succeed in capturing the known diversity of the Martian surface and variability of the Martian atmosphere, and successfully highlight locations with strong spectral signatures. Thus the CRISM summary products will be useful in both operations and science applications. Caveats and limitations related to the summary products and their interpretation are presented to assist with their application by the community at large.

Citation: Pelkey, S. M., et al. (2007), CRISM multispectral summary products: Parameterizing mineral diversity on Mars from reflectance, *J. Geophys. Res.*, *112*, E08S14, doi:10.1029/2006JE002831.

1. Introduction

[2] Determining the mineralogic composition of the Martian surface layer provides a means of understanding its origin and history. In turn, this knowledge is integral to understanding the climatic and geologic history of the planet as a whole. Spectroscopy is a means of obtaining such information and has been a widely used tool on missions to the red planet.

[3] The Compact Reconnaissance Imaging Spectrometer for Mars (CRISM) onboard the Mars Reconnaissance Orbiter is the most recent spectrometer to arrive at Mars. The instrument is a hyperspectral imager covering visible to near-infrared wavelengths (0.37–3.92 μm at 6.55 nm/channel) and has two modes of operation [*Murchie et al.*, 2007]. The survey mode will achieve global coverage of the planet at ~200 m/pixel in 72 selected channels. The targeted mode will acquire thousands of observations covering <1% of the surface at ~20 m/pixel in 545 channels, an unprecedented spatial resolution for hyperspectral data. As a means for rapid assessment of the vast amounts of data that CRISM will return, the team has defined summary products based on spectral parameters derived from the 72 channels that will be acquired in both survey mode and targeted observations [*Murchie et al.*, 2007]. The intention is to use the summary products derived from the survey mode data to characterize composition at the global scale and to search for areas of mineralogic interest to observe in the targeted mode, and to use the summary products derived from the targeted observations as tools for initial assessment in analysis.

[4] This paper presents the basis for the parameters and the validity of the above approach using data from the Mars Express (MEX) Observatoire pour la Mineralogie, l'Eau, les Glaces, et l'Activité (OMEGA) instrument, a visible to near-infrared imaging spectrometer with spatial and spectral coverage similar to that of CRISM [*Bibring et al.*, 2004b, 2005]. This study shows that the spectral parameter summary products succeed in capturing the mineralogic diversity of the Martian surface and, when interpreted with care, will be useful in both operations and science applications. This paper will introduce the summary products and their

[1]Department of Geological Sciences, Brown University, Providence, Rhode Island, USA.
[2]Applied Physics Laboratory, Laurel, Maryland, USA.
[3]Space Science Institute, Boulder, Colorado, USA.
[4]NASA Goddard Space Flight Center, Greenbelt, Maryland, USA.
[5]Institut d'Astrophysique Spatiale, Orsay, France.

Copyright 2007 by the American Geophysical Union.
0148-0227/07/2006JE002831

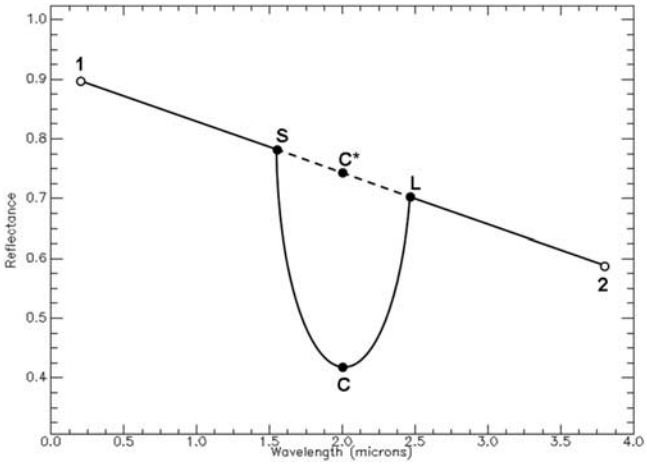

Figure 1. An explanation of some of the most common spectral parameters using an idealized spectrum. The solid line is an idealized spectrum with an absorption band superimposed on a sloped continuum. In the above example, the reflectance at the wavelength indicated by the point labeled 1 (i.e., at λ_1) is represented as R_1. Spectral slope is found by $(R_1 - R_2)/(\lambda_1 - \lambda_2)$. Band depth is found by $1 - R_C/R_{C*}$, where the point labeled C indicates the center of the absorption at λ_C, R_C is the reflectance at that wavelength, and R_{C*} is derived from the continuum fit along the dashed line and is equal to $(a*R_S + b*R_L)$, where a = 1-b and $b = (\lambda_C - \lambda_S)/(\lambda_L - \lambda_S)$.

role in spectral analysis, briefly describe the CRISM and OMEGA data sets, discuss the methodology and results of the summary product validation process, and conclude with a summary and review the limitations associated with these data products.

2. Spectral Parameters

2.1. Background

[5] The idea of utilizing parameters to analyze spectral data has been used with success in past analyses of spectral data from Mars [e.g., *Bell et al.*, 2000; *Murchie et al.*, 2000]. The concept rests on the idea that a given spectral feature can be captured by a single parameter value, which is calculated by applying an algorithm using combinations of spectral bands to the data. Each parameter is designed with a specific rationale in mind; ideally, to capture spectral features unique to a specific mineralogy. Typically the parameter value is then mapped across a region to assess spatial variations of the spectral feature, which, in turn, are interpreted as spatial variations of the associated mineralogy.

[6] The CRISM summary products will be derived from reflectances in key wavelengths and will make use of many parameters used in previous studies such as single band reflectances, reflectance ratios, spectral slope, and depths of mineralogic or gaseous absorptions. In this work, reflectance is represented by the symbol R. Surface parameters will be derived from reflectances that have undergone photometric, thermal, and atmospheric corrections; atmospheric parameters will be derived from reflectances undergoing only a simple photometric correction to normalize observations to a standard viewing geometry.

[7] Figure 1 demonstrates examples of some of the most common spectral parameters, including those mentioned above. In Figure 1, the reflectance at the wavelength indicated by the point labeled 1 (i.e., at λ_1) is represented as R_1. Spectral slope refers to the slope of the spectral continuum (the general shape of a spectrum in the absence of specific absorptions) and is represented as the change in reflectance over a given wavelength interval. The general representation of spectral slope is $\Delta R/\Delta\lambda$; in the example spectrum of Figure 1, the spectral slope is found by $(R_1 - R_2)/(\lambda_1 - \lambda_2)$. For absorptions, the depth of the absorption, or band depth, is generally represented as $1 - R\lambda/R^*\lambda$, where $R\lambda$ is the reflectance at the wavelength of the center of the absorption, and $R^*\lambda$ is the interpolated continuum reflectance at the same wavelength. The continuum level is created from a linear fit between two wavelengths from either side of the absorption that are at least local continuum levels. Using the difference of this ratio from 1 is a favored convention because it results in larger band depths for deeper absorptions. In the Figure 1 example, the band depth is $1 - R_C/R_{C*}$, where R_C is the reflectance at the center of the band, and R_{C*} is derived from the continuum fit across the band and is equal to $(a*R_S + b*R_L)$, where $a = 1 - b$ and $b = (\lambda_C - \lambda_S)/(\lambda_L - \lambda_S)$. Generally, band depth scales with the abundance of the absorbing mineral, though compounding factors such as particle size and albedo also have an effect [*Clark and Roush*, 1984].

2.2. CRISM Spectral Parameters

[8] The spectral parameters that will be used with the CRISM data are designed specifically for the CRISM wavelength regime. On the basis of a priori expectations of the composition of Mars, we began with a set of 35 parameters that primarily focused on broad mafic features expected in surface spectra and narrow hydration features expected in spectra from both the surface and the atmosphere. We then tested and evaluated these initial parameters using OMEGA data.

[9] Detailed analysis revealed that much of the spectral diversity of Mars was captured by a number of the original parameters but also that several parameters failed to show relevant variations as anticipated, and that some features identified with the full OMEGA spectral resolution were not captured at all (e.g., the sulfates and phyllosilicates reported by *Bibring et al.* [2005], *Gendrin et al.* [2005], and *Langevin et al.* [2005b]). Thus parameter formulations were reworked; some parameters were eliminated, and new parameters were added. Table 1 represents the CRISM summary products as defined at the time of publication, along with their formulations and rationale, refined according to the results of our validation efforts and the OMEGA mission itself. The outcome is a robust set of parameters capable of capturing the known atmospheric constituents and diverse surface mineralogy of Mars, as well as interesting atmospheric constituents and mineralogy yet to be detected at the planet.

[10] As the parameters in Table 1 are derived from multispectral data, the level of discrimination is limited. Most parameters have been designed to identify mineral classes rather than mineralogic species. There are 33 param-

21562202e, 2007, E8, Downloaded from https://agupubs.onlinelibrary.wiley.com/doi/10.1029/2006JE002831 by National Health And Medical Research Council, Wiley Online Library on [25/02/2025]. See the Terms and Conditions (https://onlinelibrary.wiley.com/terms-and-conditions) on Wiley Online Library for rules of use; OA articles are governed by the applicable Creative Commons License

Table 1. CRISM Spectral Parameter Summary Products[a]

Name	Parameter	Formulation[b]	Rationale
		Surface Parameters [c]	
R770	0.77 μm reflectance	R770	rock/dust
RBR	red/blue ratio	R770/R440	rock/dust
BD530	0.53 μm band depth	1 − (R530/(a*R648 + b*R440))	crystalline ferric minerals
SH600	0.60 μm shoulder height	R600/(a*R530 + b*R680)	select ferric minerals
BD640	0.64 μm band depth	1 − (R648/(a*R600 + b*R680))	select ferric minerals
BD860	0.86 μm band depth	1 − (R860/(a*R800 + b*R920))	select ferric minerals
RPEAK1	reflectance peak 1	wavelength where 1st derivative = 0 of 5th order polynomial fit to R600, R648, R680, R710, R740, R770, R800, R830	Fe mineralogy
BDI1000VIS	1 μm integrated band depth; VIS wavelengths	divide R830, R860, R890, R920 by RPEAK1 then integrate over (1 − normalized reflectances)	Fe mineralogy
BDI1000IR	1 μm integrated band depth; IR wavelengths	divide R950, R980, R1020, R1050, R1080, R1150 by linear fit from peak R between 1.3–1.87 μm to R2530 extrapolated backward to remove continuum, then integrate over (1 − continuum-corrected reflectances)	Fe mineralogy
IRA	1.3 μm reflectance	R1330	IR albedo
OLINDEX	Olivine index	(R1695/(0.1*R1050 + 0.1*R1210 + 0.4*R1330 + 0.4*R1470)) − 1	olivine will be strongly positive; based on fayalite
LCPINDEX	pyroxene index	((R1330-R1050)/(R1330 + R1050)) * ((R1330-R1815)/(R1330 + R1815)	pyroxene will be strongly positive; favors LCP
HCPXINDEX	pyroxene index	((R1470-R1050)/(R1470 + R1050)) * ((R1470-R2067)/(R1470 + R2067)	pyroxene will be strongly positive; favors HCP
VAR	spectral variance	variance of observed data from a line fit from 1.0–2.3 μm	olivine and pyroxene will have high values
ISLOPE1	−1 * spectral slope1	(R1815-R2530)/(2530-1815)	ferric coating on dark rock
BD1435	1.435 μm band depth	1 − (R1430/(a*R1370 + b*R1470))	CO_2 ice
BD1500	1.5 μm band depth	1 − (R1510/(a*R1330 + b*R1695))	H_2O ice
ICER1	1.5 μm and 1.43 μm band ratio	R1510/R1430	CO_2, H_2O ice mixtures
BD1750	1.75 μm band depth	1 − (R1750/(a*R1660 + b*R1815))	gypsum
BD1900	1.9 μm band depth	1 − (((R1930 + R1985)*0.5)/(a*R1857 + b*R2067))	H_2O
BDI2000	2 μm integrated band depth	divide R1660, R1815, R2140, R2210, R2250, R2290, R2330, R2350, R2390, R2430, R2460 by linear fit from peak R between 1.3–1.87 μm to R2530, to remove continuum, then integrate over (1 − continuum-corrected reflectances)	Fe mineralogy
BD2100	2.1 μm band depth	1 − (((R2120 + R2140)*0.5)/(a*R1930 + b*R2250))	Monohydrated minerals
BD2210	2.21 μm band depth	1 − (R2210/(a*R2140 + b*R2250))	Al-OH minerals
BD2290	2.29 μm band depth	1 − (R2290/(a*R2250 + b*R2350))	Mg,Fe-OH minerals (@ 2.3); ALSO CO_2 ice (@ 2.292)
D2300	2.3 μm drop	1 − ((CR2290 + CR2320 + CR2330)/ (CR2140 + CR2170 + CR2210)) (CR values are observed R values divided by values fit along the slope as determined between 1.8–2.53 μm (essentially continuum corrected))	hydrated min; particularly phyllosilicates
D2400	2.4 μm drop	1 − ((CR2390 + CR2430)/ (CR2290 + CR2320)) (CR values are observed R values divided by values fit along the slope as determined between 1.8–2.53 μm (essentially continuum corrected))	hydrated min; particularly sulfates
ICER2	gauge 2.7 μm band	R2530/R2600	CO_2 ice will be $\gg$ 1; H_2O ice and soil will be $\sim$1
BDCARB	2.33 & 2.53 μm band depth	1 − (sqrt [(R2330/(a*R2230 + b*R2390)) *(R2530/(c*R2390 + d*R2600))])	carbonate overtones
BD3000	3 μm band depth	1 − (R3000/(R2530*(R2530/R2210)))	H_2O
BD3100	3.1 μm band depth	1 − (R3120/(a*R3000 + b*R3250))	H_2O ice
BD3200	3.2 μm band depth	1 − (R3320/(a*R3250 + b*R3390))	CO_2 ice
BD3400	3.4 μm band depth	1 − ((a*R3390 + b*R3500)/(c*R3250 + d*R3630))	carbonates; organics
CINDEX	gauge 3.9 μm band	(R3750 + (R3750-R3630)/(3750-3630) * (3950-3750))/R3950 − 1	carbonates
		Atmospheric Parameters [d]	
R410	0.41 μm reflectance	R410	unmodeled clouds/hazes
IRR1	IR ratio 1	R800/R1020	aphelion ice clouds vs. seasonal or dust
BD1270O2	1.265 μm band	1 − ((a*R1261 + b*R1268)/(c*R1250 + d*R1280))	O_2 emission; inversely correlated with high altitude water; signature of ozone
BD1400H2O	1.4 μm band depth	1 − ((a*R1370 + b*R1400)/(c*R1330 + d*R1510))	H_2O vapor
BD2000CO2	2 μm band	1 − (R2010/(a*R1815 + b*R2170))	atmospheric CO_2

21562202e, 2007, E8, Downloaded from https://agupubs.onlinelibrary.wiley.com/doi/10.1029/2006JE002831 by National Health And Medical Research Council, Wiley Online Library on [25/02/2025]. See the Terms and Conditions (https://onlinelibrary.wiley.com/terms-and-conditions) on Wiley Online Library for rules of use; OA articles are governed by the applicable Creative Commons License

Table 1. (continued)

Name	Parameter	Formulation[b]	Rationale
BD2350	2.35 μm band depth	1 − ((a*R2320 + b*R2330 + c*R2350)/(d*R2290 + e*R2430))	CO
IRR2	IR ratio 2	R2530/R2210	aphelion ice clouds vs. seasonal or dust
BD2600	2.6 μm band depth	1 − (R2600/(a*R2530 + b*R2630))	H_2O vapor
R2700	2.70 μm reflectance	R2700	high aerosols
BD2700	2.70 μm band depth	1 − (R2700/(R2530*(R2530/R2350)))	CO_2; atmospheric structure (accounts for spectral slope)
IRR3	IR ratio 3	R3750/R3500	aphelion ice clouds vs. seasonal or dust

[a]Wavelength references in nm.
[b]The letters "a," "b," "c," "d," and "e" in band depth formulations represent fractional distances between wavelengths wavelength; for example, given BD_C, a band depth at a central wavelength C with nearby continuum points defined at shorter and longer wavelengths S and L: $BD_C = 1 - R_C/(a*R_S + b*R_L)$, where $a = 1 - b$ and $b = (\lambda_C - \lambda_S)/(\lambda_L - \lambda_S)$.
[c]To be derived from atmospherically, thermally, and photometrically corrected reflectances.
[d]To be derived from photometrically corrected reflectances.

eters related to surface mineralogy, which focus on features produced by mafic minerals, secondary alteration products (phyllosilicates, sulfates, carbonates), and ices, and 11 atmospheric parameters that focus on features related to gases and aerosols, primarily carbon monoxide and dioxide, ice clouds, water vapor, and atmospheric dust. The calculation of these 44 parameters requires observations at 72 key wavelengths (not equally spaced) and drove the selection of the wavelengths to be retrieved in the CRISM survey mode operation.

[11] Most parameters have been formulated to scale with abundance such that, to first order, larger parameter values indicate higher concentrations; however, the actual relationship is somewhat more complex. Features in reflectance spectra are influenced by a number of factors beyond abundance. Factors such as surface texture, particle size, grain size within particles, intimate mixtures of materials, layering of materials resulting from surface coatings or chemically altered surface rinds, and spatial heterogeneity within the observed field of view all have the potential to combine in ways that result in a similar band shape for very different physical surfaces [e.g., *Pieters*, 1983; *Hapke*, 1993; *Clark*, 1999; *Mustard and Sunshine*, 1999; *Johnson et al.*, 2004]. The effects of such factors can manifest themselves in a number of ways, at times resulting in misleading trends amongst the parameters such as correlations with albedo. For these reasons, it is nontrivial to convert parameters such as band depth to quantitative abundances. However, to first order, it is valid to use the parameters as qualitative indicators of the location and relative abundance of interesting spectral signatures.

3. Related Data

3.1. CRISM Data Products

[12] A detailed description of the survey and targeted operation modes of CRISM mentioned above can be found in the work of *Murchie et al.* [2007]. Worthy of mention here however, are the products that will result from each observation mode. Data from the survey mode will be used to create Multispectral Reduced Data Records (MRDR), a standard product that will consist of multiple observations of multispectral survey data mosaicked into a map tile, $\sim 5^\circ \times 5^\circ$ at the equator. Global coverage of these data will be built up during the mission and mapped into a global pattern of such tiles, forming the major data product from survey mode observations [*Murchie et al.*, 2007]. Each tile will consist of a number of layers including data in units of radiance, surface I/F, and summary products, as well as geometry and detector information relevant to the generation of the included layers. Targeted mode observations will result in Targeted Reduced Data Records (TRDR), a standard product with image data converted to units of radiance [*Murchie et al.*, 2007]. This data can also then be used to produce surface I/F TRDRs as well as a multiband image of summary products derived using the same channels acquired in the multispectral survey mode but at the higher spatial resolution of the TRDR [*Murchie et al.*, 2007].

3.2. OMEGA

3.2.1. Instrument and Major Findings

[13] OMEGA is a visible to near-infrared imaging spectrometer with three detectors that cover the wavelength range of 0.35–5.1 μm in 352 contiguous channels with sampling ranging from 7–20 nm/channel [*Bibring et al.*, 2005]. The spatial resolution of the data varies between 300 m and 4.8 km per pixel depending on the pericenter altitude of MEX's highly elliptical orbit. The instrument has achieved near global coverage and has revealed evidence for a wide diversity of materials.

[14] Consistent with past investigations [*Christensen et al.*, 2001; *Mustard et al.*, 1997], the most widely distributed mineral detected by OMEGA is Fe-bearing pyroxene [*Bibring et al.*, 2005]. Refining past results, OMEGA has identified the presence of both low- and high-calcium pyroxenes (LCP and HCP) as well as smaller distributions of olivine-enriched material [*Bibring et al.*, 2005; *Mustard et al.*, 2005]. LCP-rich areas dominate the ancient Noachian crust, HCP-rich areas typically occur in more recent lava flows, and olivine-rich material is found within crater floors and rims, and proximal to large impact basins [*Mustard et al.*, 2005]. OMEGA has also detected a number of localized distributions of two types of hydrated minerals: phyllosilicates, associated with ancient Noachian-aged terrain [*Bibring et al.*, 2005; *Poulet et al.*, 2005], and sulfates, found in layered deposits within Valles Marineris, extended deposits exposed from beneath younger units, and in the dark dunes of the northern polar cap [*Bibring et al.*, 2005; *Gendrin et al.*, 2005; *Langevin et al.*, 2005b].

[15] These findings have dramatically increased our understanding of the types and distributions of minerals on the surface of Mars and have resulted in a new percep-

21562202e, 2007, E8, Downloaded from https://agupubs.onlinelibrary.wiley.com/doi/10.1029/2006JE002831 by National Health And Medical Research Council, Wiley Online Library on [25/02/2025]. See the Terms and Conditions (https://onlinelibrary.wiley.com/terms-and-conditions) on Wiley Online Library for rules of use; OA articles are governed by the applicable Creative Commons License

tion of the planet's surface composition [*Bibring et al.*, 2005, 2006]. The similar spectral and spatial coverage of OMEGA and CRISM has provided us with an ideal opportunity to use this data set to evaluate and refine the multispectral mapping strategy set forth for CRISM operations.

3.2.2. Parameter Derivation from OMEGA Data

[16] OMEGA data were converted from instrument units to apparent I/F using standard processing approaches prior to calculating the spectral parameters. We assumed a Lambertian surface and divided the data by the cosine of the incidence angle for a photometric correction. Additionally, if calculating surface parameters, we applied a simple but efficient correction for atmospheric transmission assuming that the surface and atmospheric contributions are multiplicative, and that the atmospheric contribution follows a power law variation with altitude [*Bibring et al.*, 1989]. (Using an observation crossing Olympus Mons, an empirical spectrum for the Martian atmosphere has been derived from the OMEGA data set. The atmospheric contribution to a given observation is then removed by dividing the spectrum of interest by the empirical atmospheric spectrum, scaled by the strength of the CO_2 atmospheric absorption in the given observation. See *Mustard et al.* [2005] for more discussion.) The data have not been corrected for possible thermal contributions to the signal; due to specific complexities of the OMEGA data set, a systematic thermal correction has yet to be derived for all observations [*Jouglet et al.*, 2007]. Of the 44 spectral parameters, 12 use wavelengths longer than 2.5 μm (see Table 1) where this issue has the potential to affect the data. Thus these long-wavelength parameters have not been fully evaluated. Avoiding known problem channels in the OMEGA data (dead and hot channels, etc.), we selected OMEGA wavelength channels closest to the CRISM multispectral wavelengths referred to in Table 1, and calculated spectral parameters for every pixel of every OMEGA observation.

4. Products Used in Analysis

4.1. Surface Parameter Products

[17] One of the objectives of this work was to examine the usefulness of the CRISM strategy to analyze mosaicked map tiles of the multispectral parameters to identify areas of mineralogical interest [*Murchie et al.*, 2007]. To do this, we generated a comparable product using the OMEGA data. Using the accompanying geometry information, surface parameters derived from each OMEGA observation were mapped into global grids covering $-90°$ to $90°$ in latitude and $-180°$ to $180°$ in longitude. CRISM global products will be produced with a consistent resolution of 256 pixels per degree (ppd) ($\sim$235m/pix at the equator); however, OMEGA data average a spatial resolution of $\sim$2 km/pix so we chose a grid resolution of 32 ppd for this analysis.

[18] Our grids include OMEGA data through orbit 2395, acquired in late November 2005 at a solar longitude (Ls, or seasonal date) of 329.4°. As OMEGA started acquiring data in January 2004 at Ls = 330.1°, this subset of the data represents observations over a full Martian year. However, because of the decision to grid at 32 ppd, we chose to exclude parameters derived from the highest resolution (16-pixel wide) OMEGA observations as the grid spacing is insufficient to capture the details of these observations. (To account for the varying spatial resolution of the remaining data, the highest resolution observations are gridded on top in instances of overlapping observations.) In addition, we exclude data observed with incidence angles >70° and emergence angles >20° so that only the highest quality observations have been included in the grids.

[19] Our objective was to produce "frost-free" surface maps. Therefore, to minimize the effects of seasonal frosts in the polar regions, we also applied a solar longitude constraint to latitudes poleward of 60° N and 60°S restricting gridded data to summer-month acquisitions. Northern summer was restricted to Ls = 105°–165°; southern summer was restricted to Ls = 290°–350°. These solar longitude bounds are fairly conservative and were determined from the OMEGA data itself by limiting data to frost-free surfaces as distinguished by the absence of high-albedo seasonal frost. This technique results in an obvious boundary at ±60° latitude (see Figure 2), but eliminates the dramatic seasonal variations in the polar regions and results in what we refer to as the "unfiltered" global products (see Figure 2).

[20] However, as can be seen in Figure 2a, surface frost and uncorrected atmospheric clouds continue to interfere with some of the OMEGA observations between ±60° latitude, where no seasonal constraints have been applied. In an attempt to further reduce the interference from frost and clouds without losing significant coverage, we have devised a filtering process based on parameters that gauge the presence of H_2O and CO_2 ice, respectively, BD1500 and BD1435 (see Table 1). In this process, pixels with BD1500 or BD1435 values greater than 2% are not included in the gridded product and we refer to these products as "filtered." This technique works surprisingly well at producing "frost-free" gridded products, but it is important to note that this technique does not distinguish between atmospheric and surface ice, so both are filtered out. Consequently, not only are interfering frosts and ices removed in the filtered products, but so are the perennial polar caps, a result not necessarily desired (see Figures 3a and 3b). To combat this effect, we focus on the "unfiltered" grids that do not employ this technique when examining parameters related to the presence of water or ices.

[21] Global coverage of the OMEGA data in our gridded products is best represented by the infrared albedo parameter (IRA) seen in Figures 2a and 3a. Coverage in the "unfiltered" maps is $\sim$82% and coverage in the "filtered" maps is $\sim$78%.

4.2. Atmospheric Parameter Products

[22] The global grid format described above is not as useful for the atmospheric parameters listed in Table 1 because it does not display seasonal dependencies important for atmospheric phenomena. Typically, seasonal and latitudinal variations are more important than longitudinal variations for atmospheric properties, so a more scientifically useful product is a longitudinally averaged plot of the parameter as a function of latitude and time (or season). For our products, we average values at all longitudes for 5° bins of latitude and 5° bins of solar longitude (Ls, or seasonal date). Additionally, since seasonal variations and clouds are of interest, no constraints or filtering based on solar longitude or the presence of ices has been applied. An

21562202e, 2007, E8, Downloaded from https://agupubs.onlinelibrary.wiley.com/doi/10.1029/2006JE002831 by National Health And Medical Research Council, Wiley Online Library on [25/02/2025]. See the Terms and Conditions (https://onlinelibrary.wiley.com/terms-and-conditions) on Wiley Online Library for rules of use; OA articles are governed by the applicable Creative Commons License

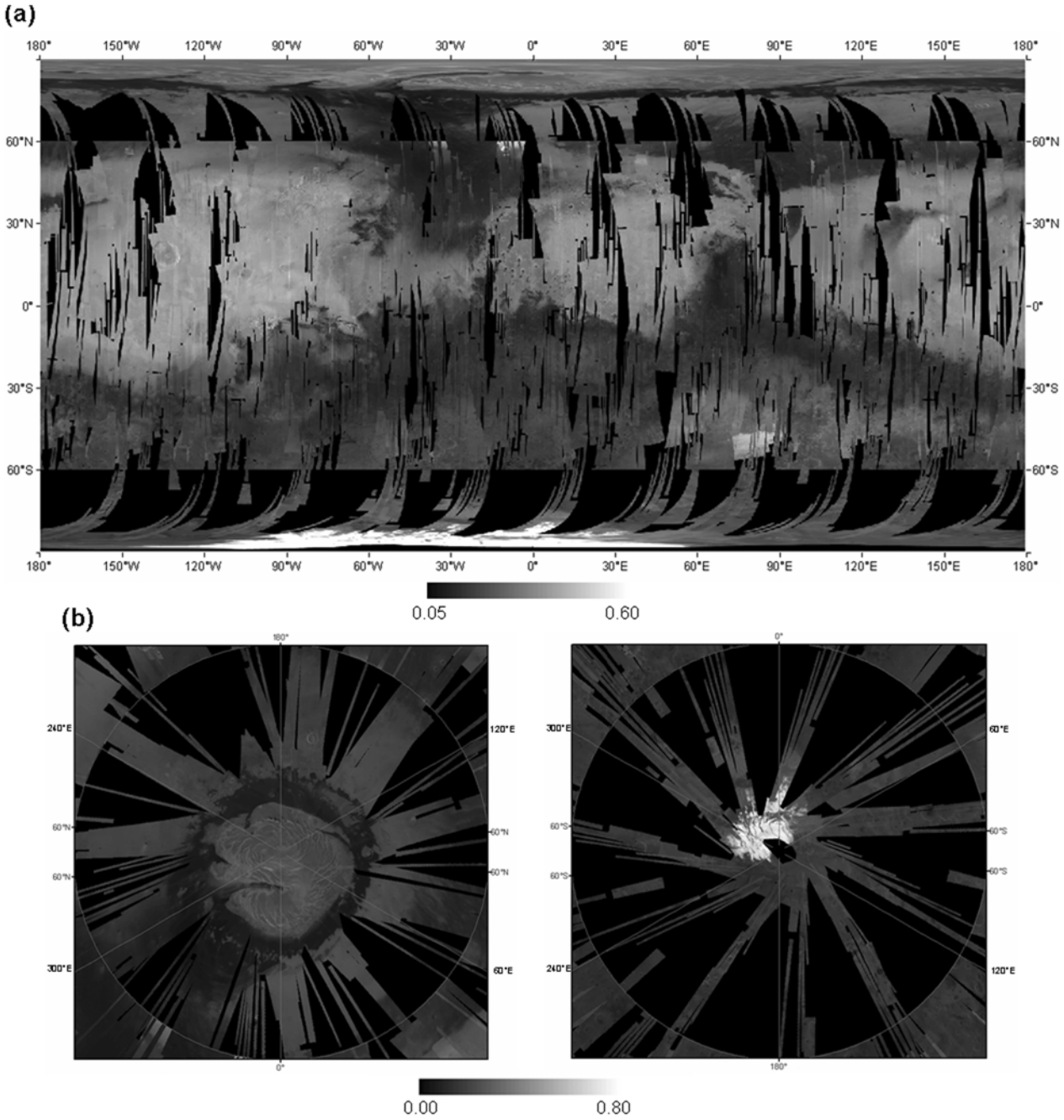

Figure 2. The "unfiltered" global grid of the infrared albedo parameter, IRA, from Table 1 as derived from OMEGA data and described in the text (swath widths vary due to MEX's elliptical orbit). (a) Global coverage. Sharp boundaries seen at ±60° latitude result from reduced coverage at poleward latitudes due to seasonal constraints imposed in the gridding process restricting data to summer-month acquisitions. No seasonal constraints were imposed for latitudes less than ±60°; as a result, interference due to seasonal surface frost can be seen at high latitudes within this area, particularly in Acidalia and Hellas. Global coverage is ∼82%. (b) Polar projections (right) from the North Pole down to 60°N and (left) from the South Pole down to −60°N.

21562202e, 2007, E8, Downloaded from https://agupubs.onlinelibrary.wiley.com/doi/10.1029/2006JE002831 by National Health And Medical Research Council, Wiley Online Library on [25/02/2025]. See the Terms and Conditions (https://onlinelibrary.wiley.com/terms-and-conditions) on Wiley Online Library for rules of use; OA articles are governed by the applicable Creative Commons License

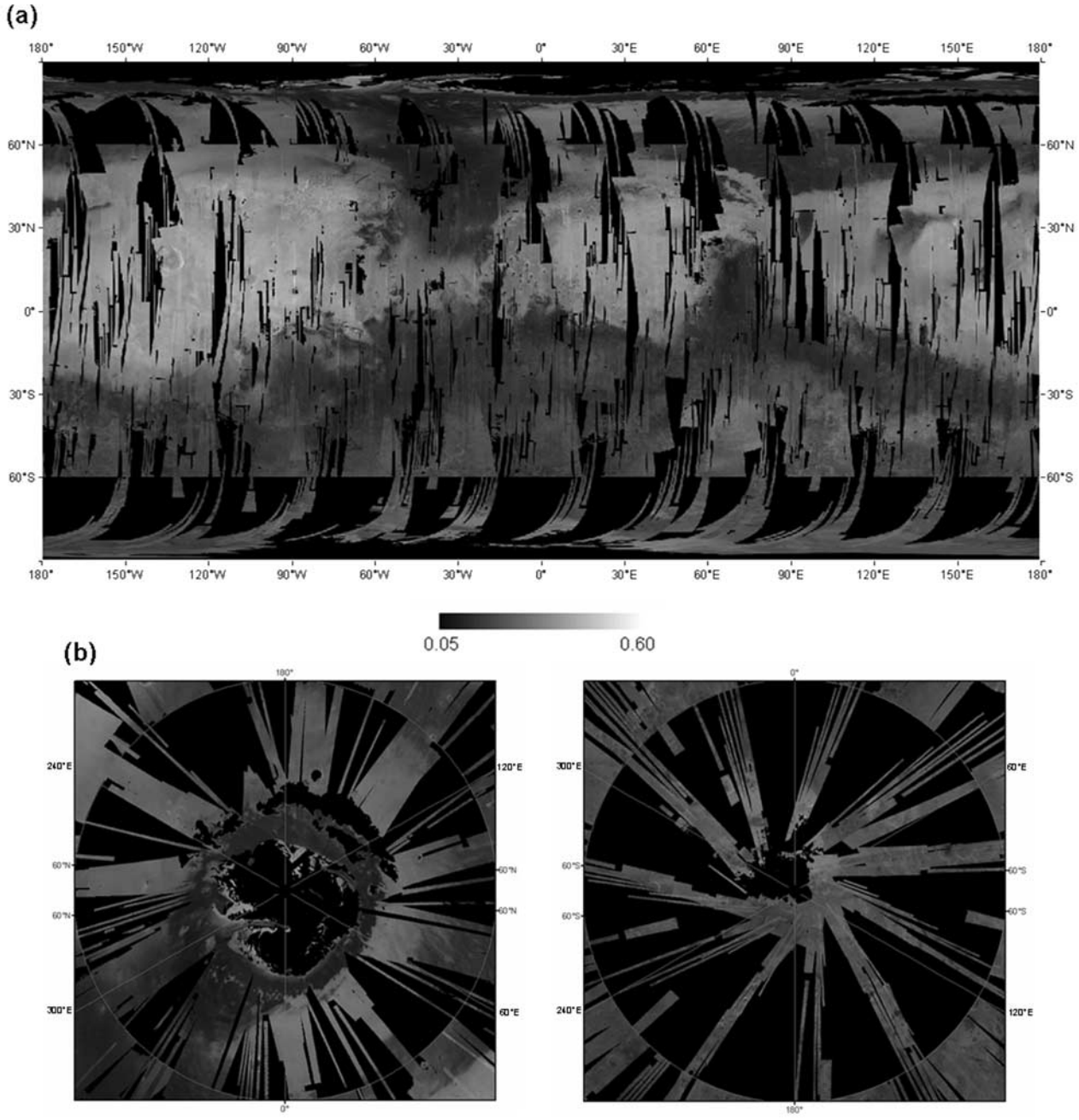

Figure 3. The "filtered" versions of grids shown in Figure 2. Data with surface frost or ice seen in Figure 2, including the polar caps, have been removed from the grid using the simplified filtering process explained in the text. (Occurrences of filtering can be identified by jagged edges and/or obviously missing pixels.) Global coverage is ~78%. Scale applies to both Figure 3a and Figure 3b.

example of such a plot showing water vapor abundance as indicated by the parameter BD1400H2O is shown in Figure 4 and discussed in more detail below.

5. Results

5.1. Initial Assessment

[23] The objective of this work is to test the stability of the multispectral parameters that will be used by CRISM and the strategy to use gridded products of these parameters to consistently identify mineralogically interesting areas. A comprehensive analysis of the global scale mineralogy of Mars using OMEGA data is being pursued by the OMEGA team [*Poulet et al.*, 2007]. However, before examining the usefulness of the summary products, we first wanted to be certain that the CRISM multispectral mode would sample the surface at sufficient spectral resolution to capture important compositional variations. Figure 5a shows hyperspectral lab data of minerals observed on the Martian surface over the CRISM wavelength range; Figure 5b shows the same data resampled to the CRISM multispectral wavelengths referred to in Table 1. Upon examination of the spectra in Figure 5b, it

21562202e, 2007, E8, Downloaded from https://agupubs.onlinelibrary.wiley.com/doi/10.1029/2006JE002831 by National Health And Medical Research Council, Wiley Online Library on [25/02/2025]. See the Terms and Conditions (https://onlinelibrary.wiley.com/terms-and-conditions) on Wiley Online Library for rules of use; OA articles are governed by the applicable Creative Commons License

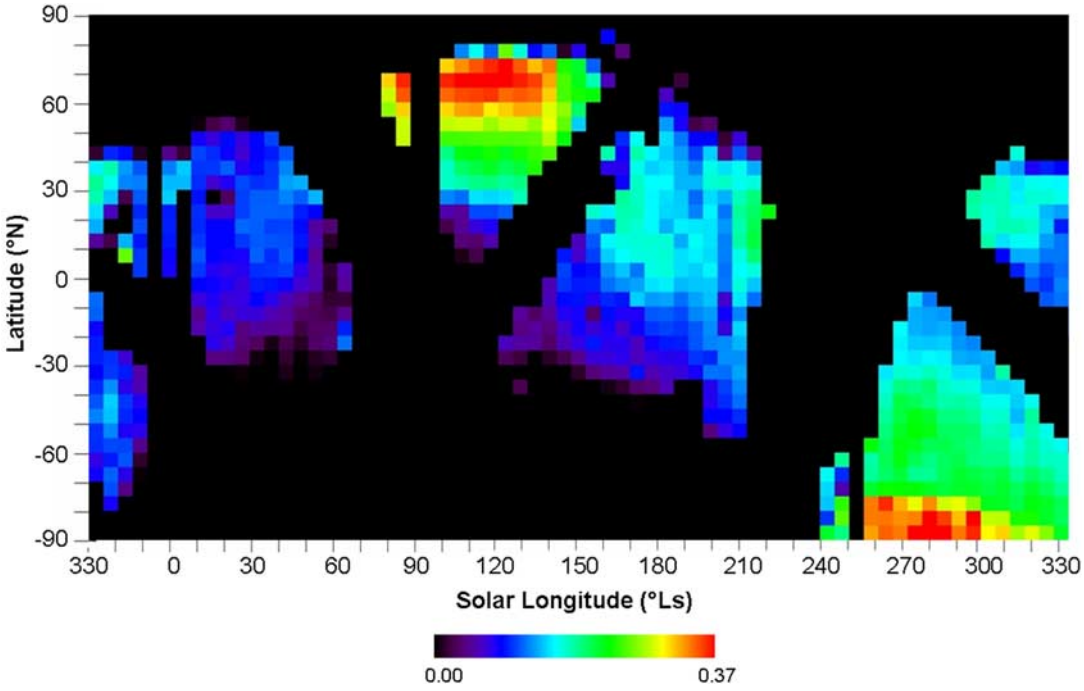

Figure 4. A plot of longitudinally averaged values of the 1.4 μm band depth parameter, BD1400H20, shown as a function of solar longitude (Ls, or seasonal date), and latitude. BD1400H2O gauges absorption due to water vapor. Latitude and Ls are binned at 5°.

is clear that the multispectral data retain the general spectral shape and key spectral properties of the data in Figure 5a, confirming that the CRISM multispectral data will be able to capture mineral diversity at the Martian surface. With this result verified, we then examined whether spectral parameters could sufficiently capture the observed spectral variations.

[24] We find that the summary products succeed in capturing the known diversity of the Martian surface and variability of the Martian atmosphere, but that the individual parameters vary in utility. Of the surface parameters, the most robust are those that highlight mafic mineralogy, hydrated silicates and sulfates, and surface ices. The least robust are those tailored for narrow absorptions or those that span atmospheric absorptions, which often show variations with time indicating that the simplistic atmospheric correction that has been applied to the data has not accurately accounted for the gasses and aerosols present in the observation. Of the atmospheric parameters, those formulated to gauge the presence of gases, which have relatively narrow, well-defined spectral features are more successful than those formulated to detect aerosols, which tend to have broader spectral features not as well captured by the multispectral approach.

[25] Even the most robust parameters, however, are susceptible to false positives. Therefore regions of interest identified in parameter products were typically evaluated using several methods and verified with the hyperspectral OMEGA data. Through this regular validation process, we developed quantitative thresholds for each parameter, values above which are assumed to reflect a robust detection. Examples in this paper make use of these thresholds, which can be found in scale bars and captions, but we note that these values reflect the capacity of a given parameter to resolve a spectral feature, a characteristic that can be dependent on a number of time-varying and instrument-specific factors such as the quality of a given observation or data set. Therefore we note that thresholds determined from the OMEGA data set may not apply to parameters derived from the CRISM data set. The only way to know what threshold values will be useful with the CRISM data is through the same verification and validation process used in this work. We continue our discussion with examples of parameters that provide valid information at OMEGA spectral and spatial resolution.

5.2. Surface Mineralogy

5.2.1. Mafic Minerals

[26] Mafic materials (i.e., those with minerals rich in magnesium and iron, such as basalt) are well distinguished by our parameters and produce grids with mineralogic distributions obvious at the global scale. Three of the most useful mafic parameters are those designed to detect olivine, low-calcium pyroxenes, and high-calcium pyroxenes, OLINDEX, LCPINDEX, and HCPINDEX respectively, which are based on characteristic absorptions in the 1 and 2 μm region (see Table 1 and related reference spectra in Figure 6). Figure 7 shows a color combination image with OLINDEX in the red channel, LCPINDEX in the green channel, and HCPINDEX in the blue channel, a display technique we have found particularly useful for evaluating closely related parameters such as these.

5.2.1.1. Pyroxenes

[27] Figure 7 shows the southern highlands to be rich in pyroxenes in both volcanic regions and the ancient crust; relative proportions of LCP and HCP vary across the region (as seen by variations in the shades of green and blue). The highest concentrations of LCP (green) occur throughout the

21562202e, 2007, E8, Downloaded from https://agupubs.onlinelibrary.wiley.com/doi/10.1029/2006JE002831 by National Health And Medical Research Council, Wiley Online Library on [23/02/2025]. See the Terms and Conditions (https://onlinelibrary.wiley.com/terms-and-conditions) on Wiley Online Library for rules of use; OA articles are governed by the applicable Creative Commons License

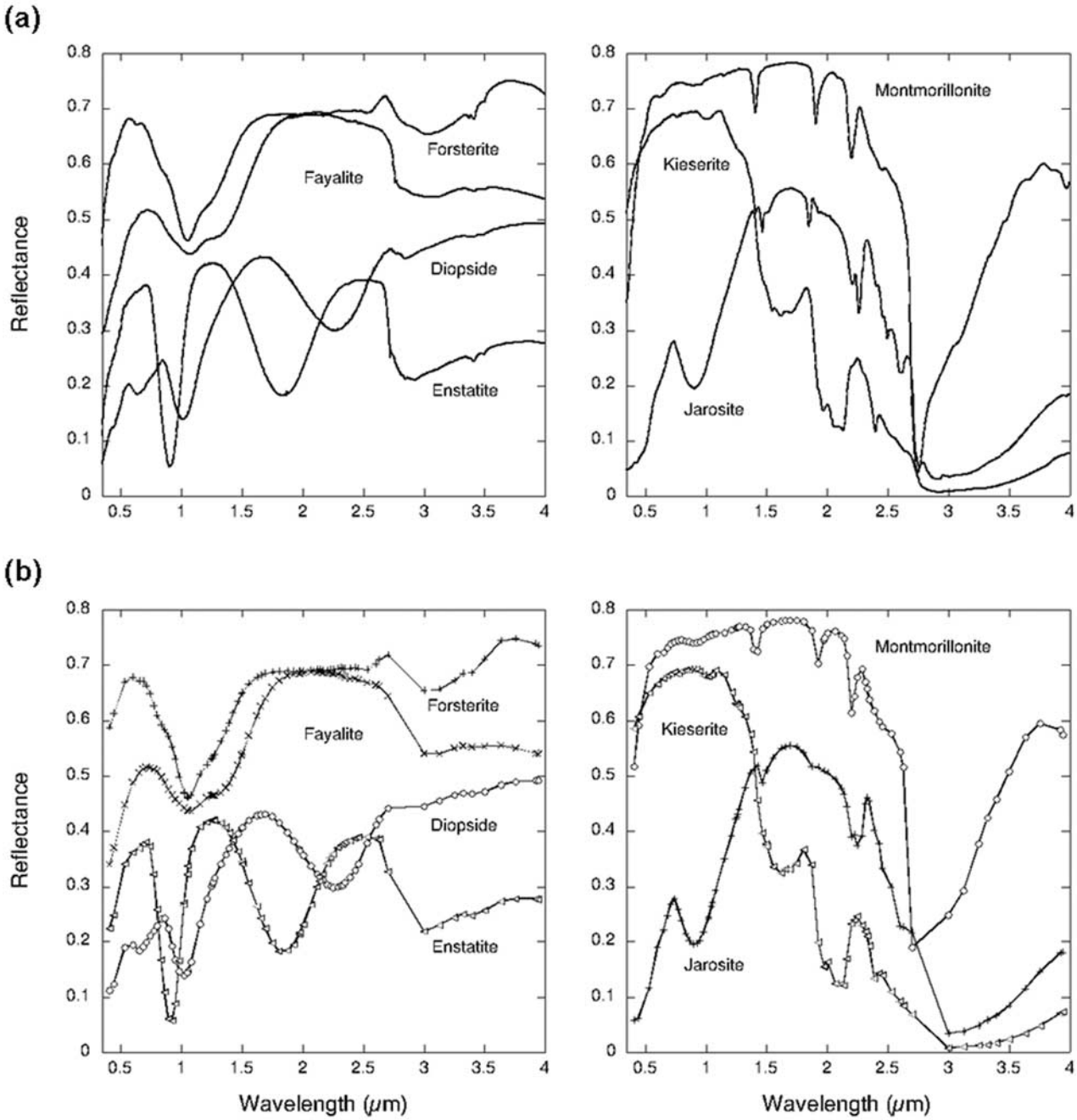

Figure 5. (a) Examples of hyperspectral lab data of mafic minerals across the CRISM wavelength range. Spectra represent a subset of mineralogy observed on the surface of Mars. The panel on the left shows spectra from mafic materials (forsterite: Mg-rich olivine; fayalite: Fe-rich olivine; diopside: high-Ca pyroxene (HCP); enstatite: low-Ca pyroxene (LCP)); the panel on the right shows spectra of phyllosilicates and sulfates (montmorillonite: Al-rich smectite clay; kieserite: monohydrated Mg-sulfate; jarosite: ferric sulfate hydroxide). (b) Multispectral version of data from Figure 5a resampled to the 72 wavelengths used for the CRISM parameters in Table 1 (symbol locations indicate wavelengths used). Results clearly retain the general spectral shape as seen in Figure 5a, indicating that CRISM multispectral observations will succeed in capturing mineral diversity at the Martian surface.

Noachian cratered terrains of the Southern Highlands, whereas HCP concentrations (blue) dominate the more equatorial volcanic regions of Hesperian age. Pyroxene signatures can also be seen at high latitudes, where they correspond to sand and dunes in the polar regions. These results complement past mapping results from Thermal Emission Spectrometer (TES) data [*Bandfield et al.*, 2000] and are in direct agreement with those from OMEGA reported by *Bibring et al.* [2005, 2006] and *Mustard et al.* [2005]. Though not visible at the scale of Figure 7, our parameter grids also highlight pyroxene detections in small outcrops in the walls and floor of Valles Marineris and high HCP

21562202e, 2007, E8, Downloaded from https://agupubs.onlinelibrary.wiley.com/doi/10.1029/2006JE002831 by National Health And Medical Research Council, Wiley Online Library on [23/02/2025]. See the Terms and Conditions (https://onlinelibrary.wiley.com/terms-and-conditions) on Wiley Online Library for rules of use; OA articles are governed by the applicable Creative Commons License

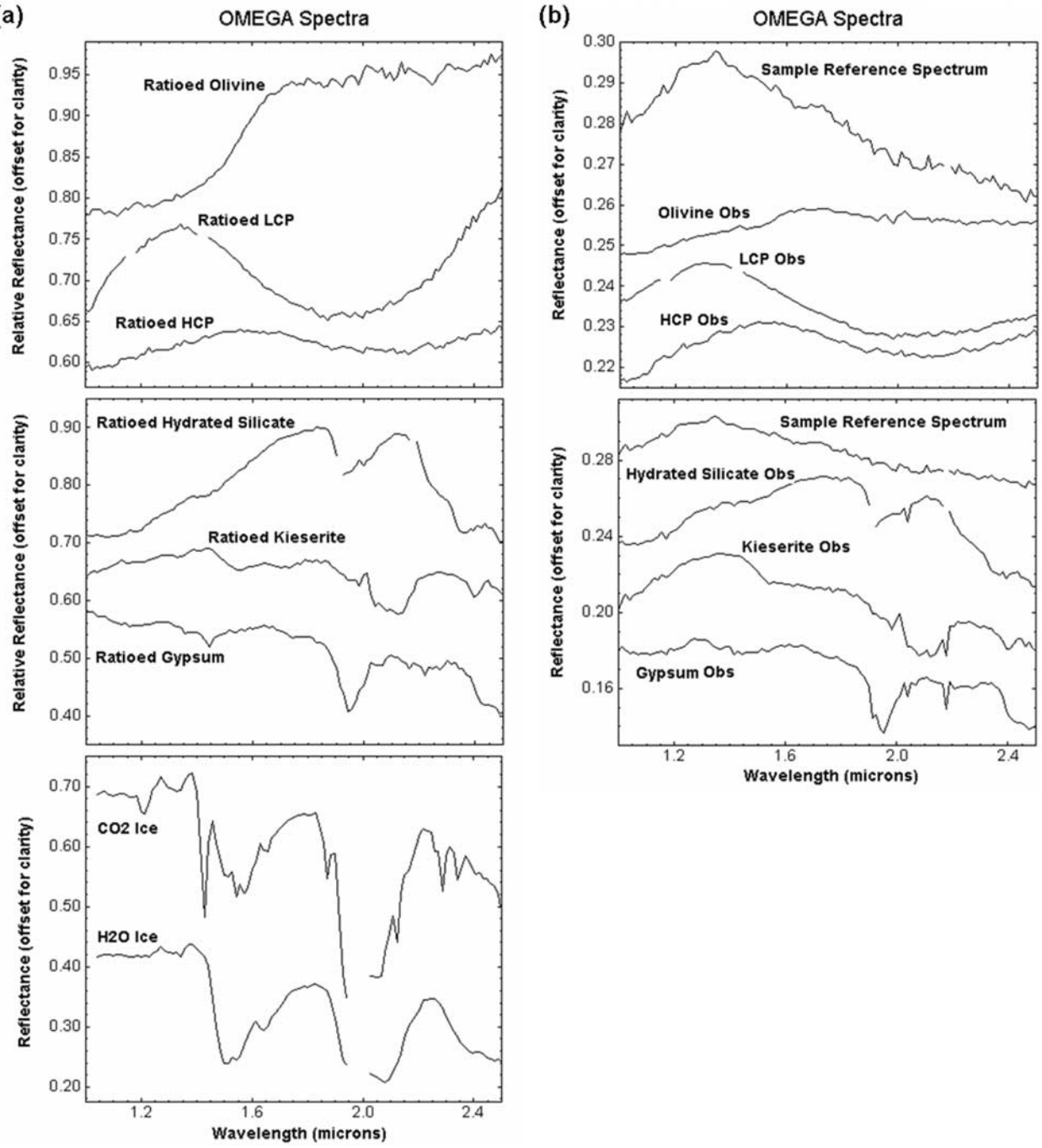

Figure 6. Figure 6a shows representative OMEGA spectra referred to throughout the text. Chosen spectra represent the mineralogic diversity that has been detected at the surface of Mars. These example spectra do not represent pure minerals, but rather spectral signatures dominated by a specific mineral species, for example: mafic material in the top panel (olivine, LCP, and HCP from Nili Fossae/Syrtis Major), hydrated minerals in the middle panel (hydrated silicate from Syrtis Major/Nili Fossae region; sulfates: kieserite from Melas Chasma, gypsum from northern polar deposits), and ices in the bottom panel (water ice and CO_2 ice from South Pole). The wavelength range shown is that of the most accurately calibrated OMEGA detector. Spectral discontinuities indicate the removal of hot or dead channels or, in the case of the ices, bands with atmospheric interference not properly accounted for by our atmospheric correction. Spectra shown as ''Relative Reflectance'' in the top two panels have been ratioed to spectrally neutral reference spectra from nearby dusty terrains to enhance spectral features of the mineral of interest. Original reflectance spectra can be seen in the associated panels on the right in Figure 6b along with a representative example of the reference spectrum. The spectral features of ices in the bottom panel are strong enough to be seen in the original reflectance spectra and did not require ratios for enhancement.

21562202e, 2007, E8, Downloaded from https://agupubs.onlinelibrary.wiley.com/doi/10.1029/2006JE002831 by National Health And Medical Research Council, Wiley Online Library on [25/02/2025]. See the Terms and Conditions (https://onlinelibrary.wiley.com/terms-and-conditions) on Wiley Online Library for rules of use; OA articles are governed by the applicable Creative Commons License

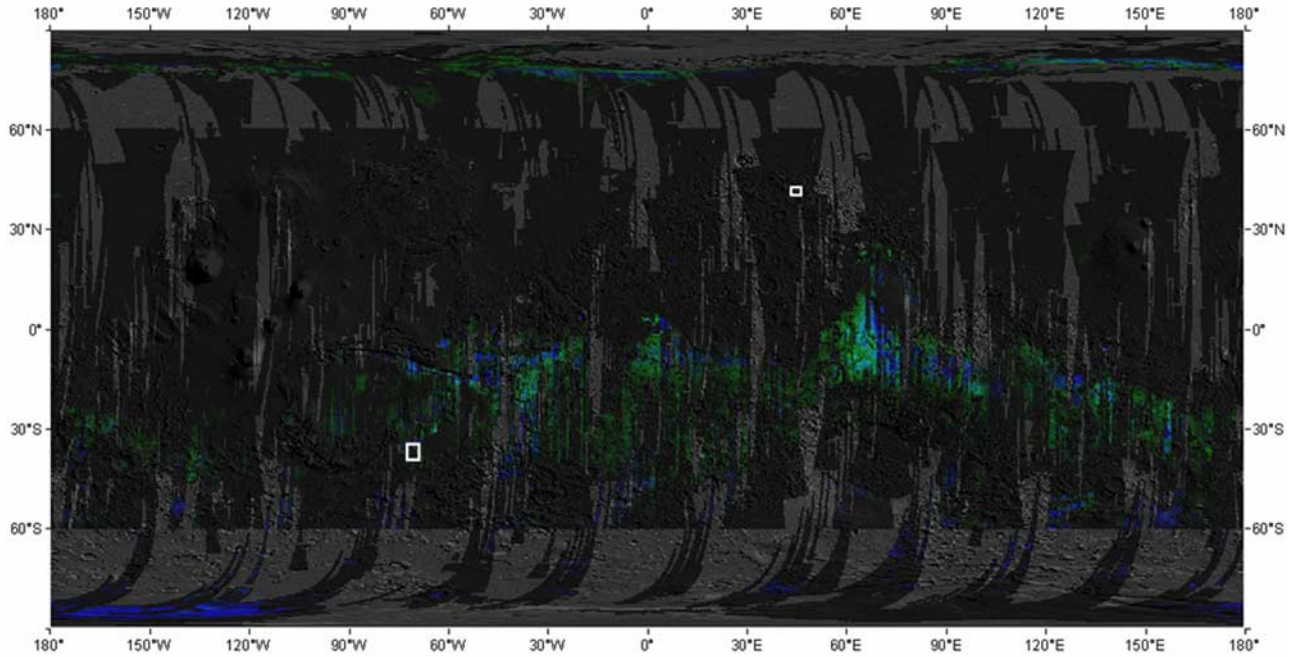

Figure 7. A color combination image of filtered global grids of the mafic parameters OLINDEX, LCPINDEX, and HCPINDEX (in the red, green, and blue channels, respectively) overlain on a muted MOLA shaded relief map for context. Color stretches are as follows: R: 0.010–0.250, G: 0.001–0.0025, B: 0.002–0.004. White boxes represent areas shown in Figure 8.

concentrations in dark sand and crater ejecta as was also reported by *Bibring et al.* [2005] and *Mustard et al.* [2005].

[28] We note that there is a slightly more variability in our parameter grids than in the maps published by the OMEGA team [*Bibring et al.*, 2005, 2006]. This result is a consequence of the different procedures used to create the products. The OMEGA-team maps are created from results produced using an approach based on the Modified Gaussian Model (MGM) [*Gendrin et al.*, 2006; *Sunshine et al.*, 1990]. It is not surprising that simplified multispectral parameters do not distinguish between pyroxenes as well as a more tailored model like MGM. Typically, it is more appropriate to think of a parameter as representing a tendency toward one mineral signature over another rather than a well-constrained detection. Therefore one would expect the multispectral grids to be less refined than maps created from MGM model results. However, the similarity in the results from each method is quite encouraging.

5.2.1.2. Olivines

[29] At the global scale of Figure 7, olivine (red) seems absent but this is because the strongest olivine signatures are found exclusively in small, localized regions. As discussed by *Bibring et al.* [2005, 2006] and *Mustard et al.* [2005], highlighted areas are seen mainly in association with volcanic rocks in and around Syrtis Major as reported in the past [*Hoefen et al.*, 2003; *Hamilton and Christensen*, 2005], as well as in crater floors and rims. Figure 8 shows examples of these regional detections from the global grid. The spatial coherence of the parameter signatures and the association with the underlying geology indicate strong spectral features associated with distinct geological units.

5.2.2. Hydrated Minerals

[30] Unlike some of the mafic parameter grids discussed above, there are no detections in the grids of parameters targeted at hydrated minerals, such as phyllosilicates and sulfates, that correspond to global scale geology. These minerals are detected in regional-scale deposits [*Bibring et al.*, 2006] and our parameter grids successfully highlight all of the areas that have previously been reported. These include the phyllosilicates reported by *Bibring et al.* [2005] and *Poulet et al.* [2005] detected in eroded outcrops near Mwarth Vallis, Nili Fossae, the southern Isidis rim, northern Hellas, and around Terra Meridiani as well as those in dark deposits within Arabia Terra, northern Syrtis Major, northern Terra Meridiani, Xanthe Terra and Lunae Planum. Also identified are the numerous sulfate detections reported by *Bibring et al.* [2005] and *Gendrin et al.* [2005] in light-toned layered deposits within Valles Marineris and in extended deposits exposed in Terra Meridiani and Aram and Iani Chaos, as well as those in the north polar dunes [*Langevin et al.*, 2005b].

[31] As with mafic minerals, the detection of hydrated minerals often relies on using multiple parameters in a complimentary manner. For example, BD1900 gauges the depth of an absorption band at ~1.9 μm due to the presence of H_2O (that which is adsorbed or structurally bound), but this information alone is insufficient to make mineralogic distinctions beyond the presence of water. Therefore we typically look to other parameters, such as D2300 and D2400, for corresponding signatures. D2300 is designed to pick up a spectral feature observed in hydrated silicates, specifically a decrease in reflectance that occurs near 2.3 μm due to absorptions related to metal-OH vibrations [*Clark et al.*, 1990]. D2400 is similar, but is more sensitive to hydrated sulfates as it gauges water-related absorption features modulated by the presence of H_2O in a sulfate lattice [*Arvidson et al.*, 2005]. Therefore, by using these three parameters in conjunction with each other, we can often

21562202e, 2007, E8, Downloaded from https://agupubs.onlinelibrary.wiley.com/doi/10.1029/2006JE002831 by National Health And Medical Research Council, Wiley Online Library on [25/02/2025]. See the Terms and Conditions (https://onlinelibrary.wiley.com/terms-and-conditions) on Wiley Online Library for rules of use; OA articles are governed by the applicable Creative Commons License

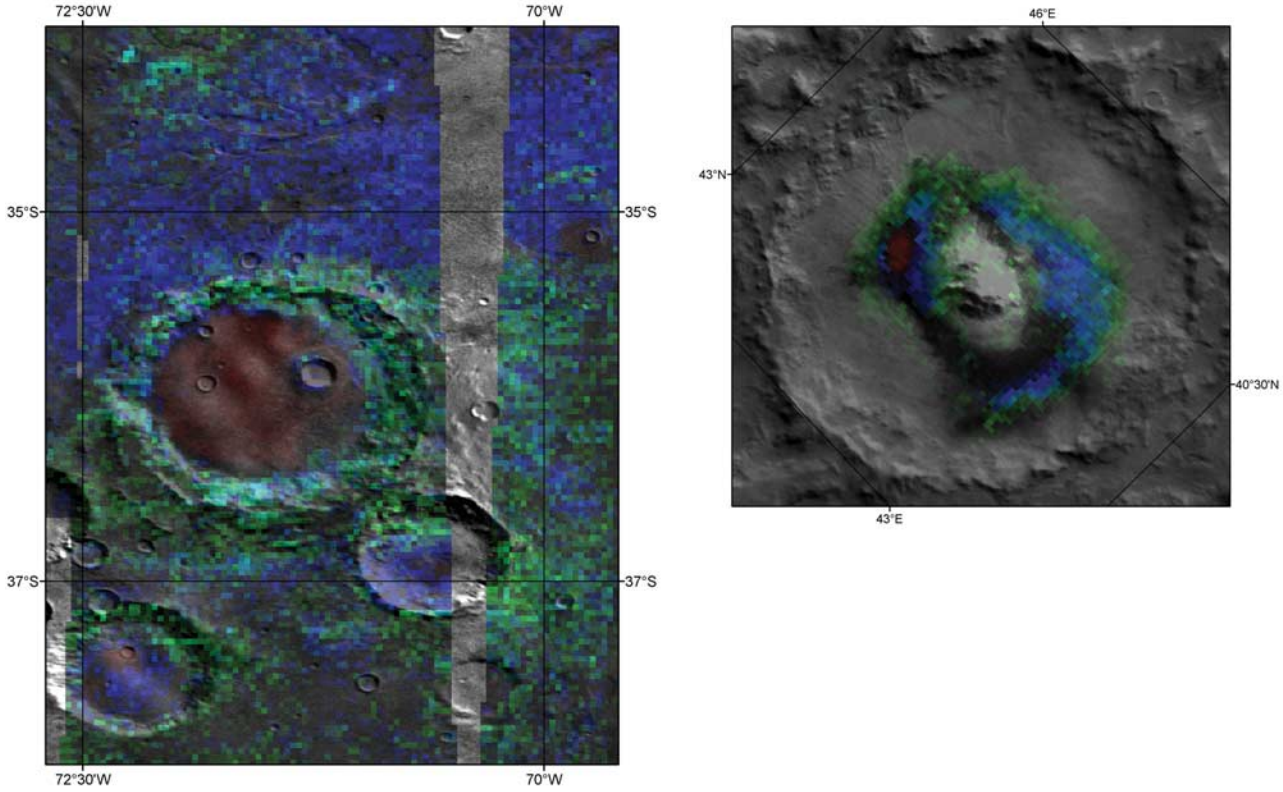

Figure 8. Regional examples from the gridded product shown in Figure 7 (backgrounds have been changed from MOLA shaded relief to MDIM2.1); see white boxes in Figure 7 for global context. Colors show local-scale variations in the distribution of mafic materials highlighting areas with a high OLINDEX seen in red.

distinguish between simply hydrated material and hydrated silicates or sulfates. Other parameters such as BD2100, which is tuned to detect shifted 1.9 μm water absorption bands modulated by monohydration within a sulfate lattice [*Gendrin et al.*, 2005; *Arvidson et al.*, 2005], can help to further refine mineral identification. Figure 9 shows an example of a color composite using BD2100, D2400, and BD1900 for Aram Chaos, a mineralogically rich area discussed in detail by *Glotch and Christensen* [2005]. The parameters indicate the presence of both mono- and polyhydrated minerals, including sulfates, in locations associated with the detection of hematite from TES [*Gendrin et al.*, 2005; *Glotch and Christensen*, 2005].

[32] Hydrated mineral detections have the added complexity of involving a parameter that has the potential to confuse water of hydration and water-ice. Although absorption bands generally shift to slightly longer wavelengths in water-ice spectra (see representative spectra in Figure 6), strong absorptions are often close enough to contribute to parameter calculations designed to detect features due to water of hydration. Thus grids of a single parameter such as BD1900 have the potential to include compounded signatures of both hydrated minerals and water-ice. A perfect example of where this can confuse detections is at the North Pole. Figure 10a shows an unfiltered grid of BD1900 over the residual north polar cap, discussed in more detail in the following section; the grid clearly shows the strongest detections over the residual cap (note: some track-to-track variations can be seen in this and other figures most often resulting from temporal variations in observational conditions such as aerosols, which are not accounted for in our simple atmospheric correction, or subtle variations in instrument response). Figure 10b shows the same grid, but has undergone the filtering process described above to remove data with ice signatures above our threshold; a new stretch has been applied to the data as well. As expected, a large fraction of the positive detections seen in Figure 10a has been removed, indicating that the signatures were due to the presence of water ice. Additionally, filtering has also isolated the signatures from the hydrated sulfate deposit in the circumpolar dunes reported by *Langevin et al.* [2005b]. Thus parameters related to water of hydration can be nonunique and require special consideration, particularly in areas where water ice has the potential to interfere.

5.2.3. Surface Ices and Frosts

[33] Although we have just discussed the confusion that the presence of water ice can cause in parameters designed to detect hydrated phases, the inverse is typically not as significant a problem. Both water ice and CO_2 ice produce unique spectral features that are well distinguished by our parameters, which allows the filtering method discussed above to work so successfully. However, when dealing with the detection of surface frosts and ices themselves, it is obviously useful to analyze grids that have not been filtered. When doing so, the most obvious detections occur in the polar regions.

[34] Unfiltered grids of the ice parameters from the summer observations at the North Pole (Ls = 105°–165°) show strong BD1500 signatures gauging the water ice band

21562202e, 2007, E8, Downloaded from https://agupubs.onlinelibrary.wiley.com/doi/10.1029/2006JE002831 by National Health And Medical Research Council, Wiley Online Library on [23/02/2025]. See the Terms and Conditions (https://onlinelibrary.wiley.com/terms-and-conditions) on Wiley Online Library for rules of use; OA articles are governed by the applicable Creative Commons License

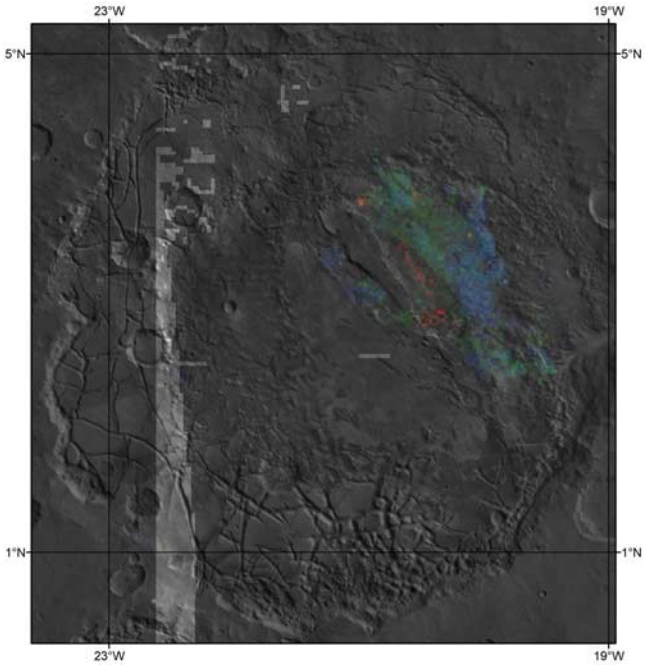

Figure 9. Aram Chaos: A color combination image of filtered grids of the hydrated mineral parameters BD2100, D2400, and D1900 (in the red, green, and blue channels, respectively) overlain on an MDIM2.1 for context. Red areas represent monohydrated material, greens, and yellows, and aquas indicate hydrated sulfates, while blues indicate nondistinct polyhydrated material. (Variations in the OMEGA pixel size and occurrences of filtering are noticeable in the coverage of the dark background values of the OMEGA data.) Color stretches are as follows: R: 0.020–0.050, G: 0.020–0.100, B: 0.020–0.075.

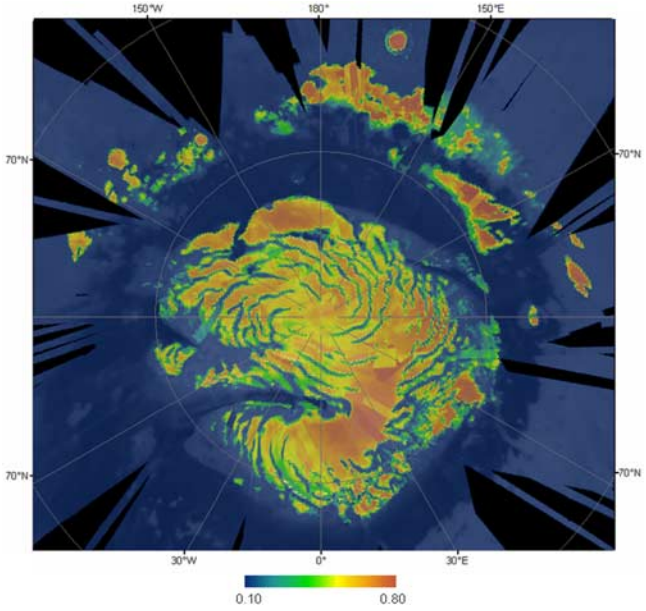

Figure 11. North Pole: An unfiltered grid of the 1.5 μm band depth parameter, BD1500, gauging water-ice absorption, from summer month acquisitions (Ls = 105°–165°) overlain on an unfiltered grid of the infrared albedo parameter (IRA).

at 1.51 μm (see Figure 11) but lack a BD1435 signature, which gauges the CO_2 ice band at 1.435 μm (see Table 1 and related reference spectra in Figure 6). These results reproduce findings from past missions that identified a large water-rich, CO_2-ice-free, residual polar cap [*Kieffer et al.*, 1976; *Kieffer and Titus*, 2001; *Bibring et al.*, 2005;

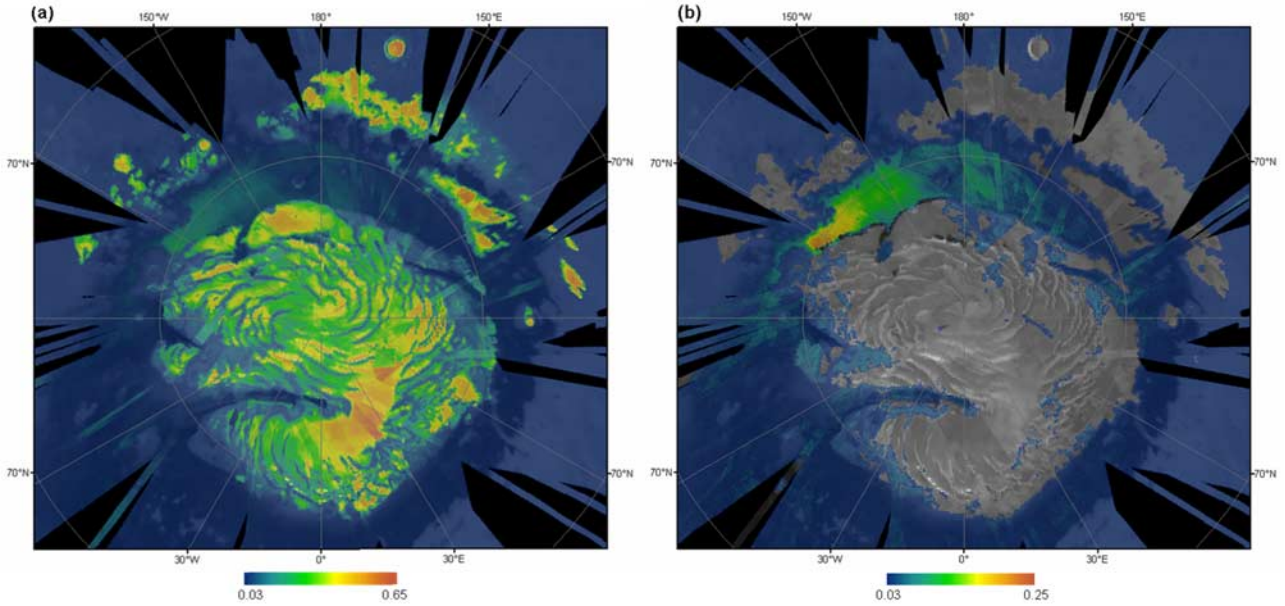

Figure 10. Grids of the 1.9 μm band depth parameter, BD1900, from summer data over the North Pole (Ls = 105°–165°). (a) Unfiltered version; the parameter is intended to gauge absorption due to water of hydration, but it is clearly detecting water-ice over the residual cap as well. (b) Filtered version of the grid in Figure 10a with a new stretch; by removing data with strong ice absorptions, we have isolated the hydrated mineral deposit in the circumpolar dunes.

21562202e, 2007, E8, Downloaded from https://agupubs.onlinelibrary.wiley.com/doi/10.1029/2006JE002831 by National Health And Medical Research Council, Wiley Online Library on [23/02/2025]. See the Terms and Conditions (https://onlinelibrary.wiley.com/terms-and-conditions) on Wiley Online Library for rules of use; OA articles are governed by the applicable Creative Commons License

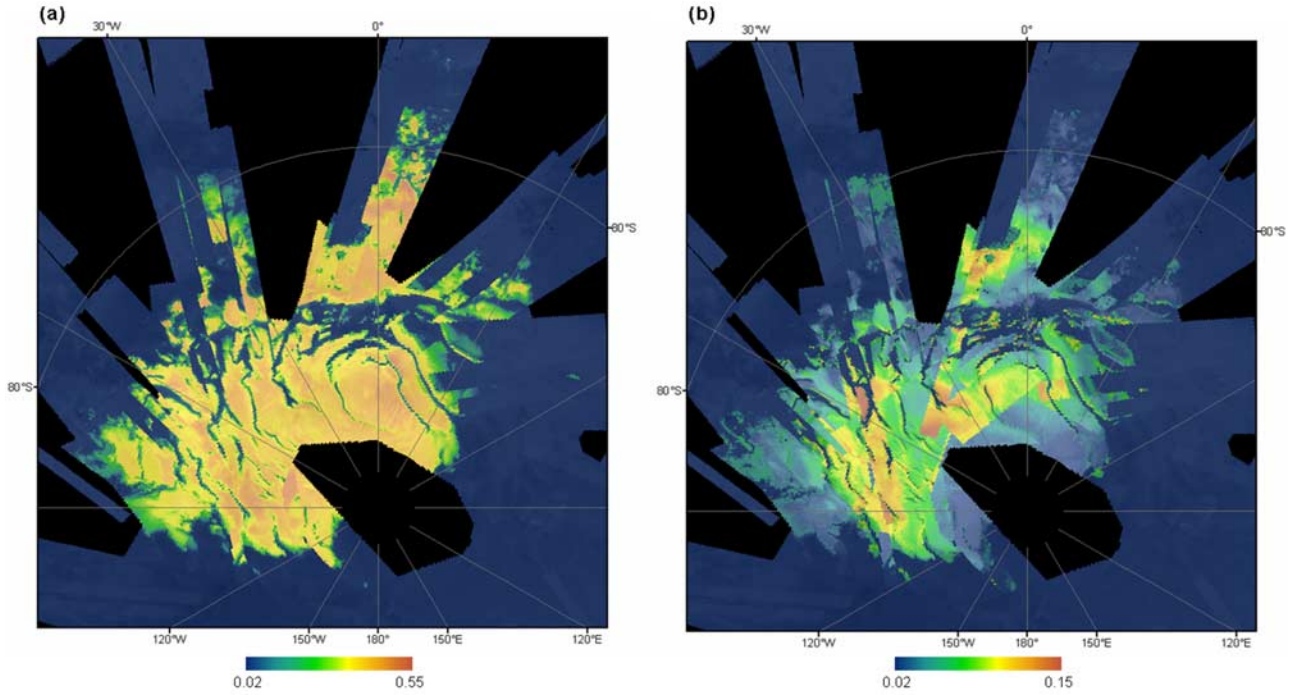

Figure 12. South Pole: Unfiltered grids of ice parameters obtained from summer month acquisitions (Ls = 290°–350°) overlain on an unfiltered grid of the infrared albedo parameter (IRA). (a) The 1.435 μm band depth parameter, BD1435, gauging CO_2-ice absorption. (b) The 1.5 μm band depth parameter, BD1500, gauging water-ice absorption.

Langevin et al., 2005a]. The distribution of BD1500 in Figure 11 is also in excellent agreement with the surface water ice map from OMEGA data published by *Langevin et al.* [2005a], further substantiating the validity of the parameters.

[35] Grids of the same parameters made from summer observations at the South Pole (Ls = 290°–350°) also show BD1500 signatures, though much subdued in comparison to the values detected in the north, as well as significant BD1435 values (see Figure 12). The BD1500 signature exhibits more spatial variation than is observed in the BD1435 grid, though both cover similar spatial extents. This is a slightly different result from those for the same area reported by *Bibring et al.* [2004a], who used initial OMEGA observations from Ls = 335°–348°. The BD1500 distribution shown in Figure 12b is similar to the water ice map from *Bibring et al.* [2004a], but our BD1435 results show a more expansive CO_2 ice distribution (see Figure 12a). We find that CO_2 ice is present in the same locations as water ice, across the residual cap (as was also seen by *Bibring et al.* [2004a] in "Unit 1"), but also in scarps around the cap and in areas tens of kilometers away from the cap ("Units 2 and 3" from *Bibring et al.* [2004a] where CO_2 ice was not observed) (see Figure 12). *Bibring et al.* [2004a] concluded that the perennial southern cap contains water ice that extends beyond the CO_2-ice-rich area, but note that the CO_2-ice might be restricted to a fairly thin layer, no more than meters in depth, which also agrees with past estimates [*Thomas et al.*, 2000]. Thus differences in our grids may simply be capturing interannual variability in the sublimation of CO_2-ice, particularly since the grids presented here include observations from slightly earlier solar longitudes as well.

5.3. Atmospheric Results

[36] Given the complexity of the relationship between surface and atmospheric contributions to the signal observed at the detector, nadir observations, such as those used to create these parameter products, are not ideal for discriminating the subtle contrast and broad-band signatures of aerosols. Nonetheless, some of the atmospheric parameters clearly show aerosol signatures.

[37] Single channel reflectances have proven to be useful. Figure 13 shows a longitudinally averaged seasonal plot of the parameter R410, the reflectance at 0.41 μm. This parameter succeeds as an indicator for the aphelion cloud belt at subtropical northern latitudes, as well as bright topographic clouds and high-altitude hazes [*Clancy et al.*, 1996, 2003]. In addition, information on dust abundance can be gained from the reflectance within the optically deep CO_2 absorption band at 2.7 μm, in the parameter R2700. Seasonal variations in the longitudinally averaged seasonal grid of R2700 (not shown here) reflect variations in the amount of dust lofted to higher altitude levels (above 30–40 km) in the atmosphere, with large increases in reflectance often associated with large-scale dust events such as often exhibited around L_S = 210° and 330°.

[38] Referred to earlier, Figure 4 shows a longitudinally averaged seasonal grid of BD1400H2O, a parameter measuring the band depth of the 1.4 μm absorption related to water vapor. Although the seasonal-latitudinal coverage is not complete, clear seasonal trends are seen including a

21562202e, 2007, E8, Downloaded from https://agupubs.onlinelibrary.wiley.com/doi/10.1029/2006JE002831 by National Health And Medical Research Council, Wiley Online Library on [25/02/2025]. See the Terms and Conditions (https://onlinelibrary.wiley.com/terms-and-conditions) on Wiley Online Library for rules of use; OA articles are governed by the applicable Creative Commons License

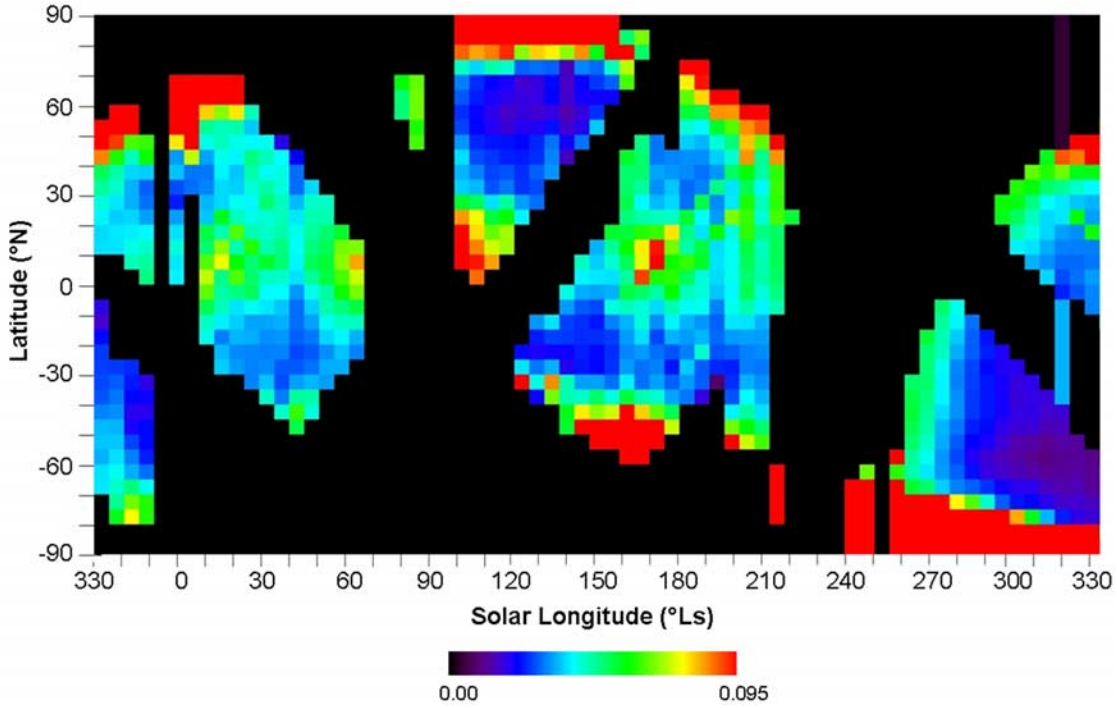

Figure 13. A plot of longitudinally averaged values of reflectance at 0.410 μm, parameter R410, shown as a function of solar longitude, or seasonal date (Ls), and latitude. R410 is used to track unmodeled clouds and hazes. Latitude and Ls are binned at 5°.

dramatic increase in band depth at mid to high latitudes in the summer hemisphere (both north and south; $L_S = \sim 90°$ for northern latitudes, and $L_S = \sim 270°$ for southern latitudes). Intermediate values are found at low latitudes between Ls = 120° and 330°, and the lowest values are observed in the Southern Hemisphere during winter. These seasonal-latitudinal trends are in agreement with results reported by *Schmitt et al.* [2005] and *Maltagliati et al.* [2006] from the hyperspectral OMEGA data and are consistent with previous ground-based and spacecraft observations [e.g., *Jakosky and Farmer*, 1982; *Smith*, 2002; *Sprague et al.*, 2003].

[39] A difficulty of working with some of the parameters designed to detect gas features is that many are uniformly distributed in the atmosphere and subject to a dependency on topography. Lower surface altitudes result in longer path lengths with larger atmospheric column densities, which can result in stronger spectral features depending on the species being studied. Therefore an in depth analysis of some of these parameters, such as BD2350, a parameter measuring the depth of an absorption feature at 2.35 μm related to carbon monoxide (CO), requires a correction for this effect. A first order correction can be made by normalizing affected parameters to BD2000CO2, an index gauging carbon dioxide (CO_2) abundance, with the intention of using BD2000CO2 as a proxy for topography. Figure 14 shows the longitudinally averaged seasonal grid of BD2350 normalized in this fashion. There appears to be a pattern of seasonal variation supporting reports of spatial and temporal variation in CO as indicated from hyperspectral OMEGA data [*Drossart et al.*, 2005], however, this normalization technique is only a coarse approximation to a true correction. A more accurate correction for the topographic dependence is required before more detailed conclusions can be drawn, but lies beyond the scope of this paper.

[40] Other atmospheric parameters are not subject to this dependency and interpretations can be made directly from the gridded products. One such parameter is BD1270O2 designed to capture oxygen (O_2) emission resulting from the photolysis of ozone (O_3). The longitudinally averaged seasonal grid of BD1270O2 (not shown here) appears to support results reported by *Zasova et al.* [2006] indicating spatial and temporal variations in O_2 emission as seen in the hyperspectral OMEGA data. However, the emission feature is narrow and not completely resolved even at the full spectral sampling of OMEGA. With a finer spectral resolution, CRISM should allow for improved characterization of this feature and the related process.

6. Caveats

[41] In order to maximize their scientific potential, the summary products need to be well understood and interpreted with care. This required us to identify, characterize, and become familiar with limitations and misleading trends of the spectral parameters. We take this opportunity to present some of the most relevant caveats encountered. This information will also benefit those who intend to work with and interpret the CRISM summary products.

[42] The surface summary products will be most representative of the surface when derived from fully corrected, accurate surface reflectances. In our examination, instances when the simple corrections applied to the OMEGA data were insufficient to completely correct atmospheric and photometric effects translated to misleading signatures in

21562202e, 2007, E8, Downloaded from https://agupubs.onlinelibrary.wiley.com/doi/10.1029/2006JE002831 by National Health And Medical Research Council, Wiley Online Library on [25/02/2025]. See the Terms and Conditions (https://onlinelibrary.wiley.com/terms-and-conditions) on Wiley Online Library for rules of use; OA articles are governed by the applicable Creative Commons License

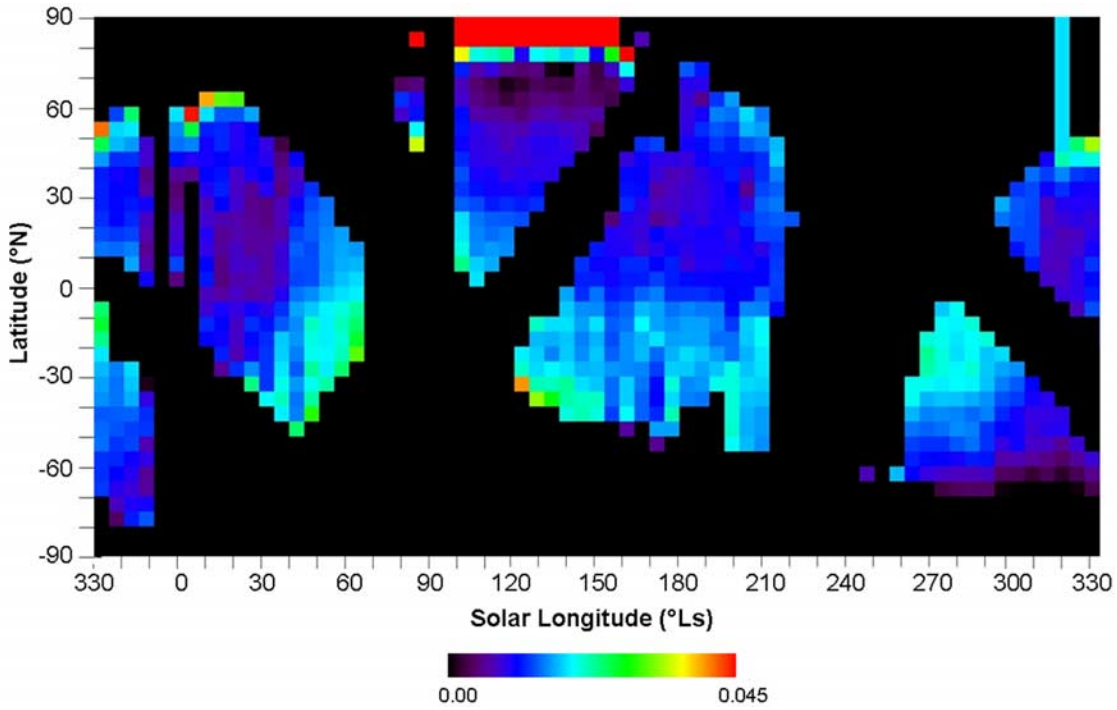

Figure 14. A plot of longitudinally averaged values of the 2.35 μm band depth parameter, BD2350, shown as a function of solar longitude, or seasonal date (Ls), and latitude. BD2350 gauges absorption due to CO; the grid has been normalized by BD2000CO2 as a first-order correction for dependence on altitude. Latitude and Ls are binned at 5°.

the parameter grids. We were able to minimize these effects through filtering processes, but only with the undesirable consequence of removing data that would have otherwise been useful had it undergone a thorough and more accurate correction. CRISM data reduction will include a systematic aerosol and gas correction converting data to surface Lambert albedo prior to deriving the multispectral summary products [*McGuire et al.*, 2006]. However, even when using accurate reflectances, instrumental noise can produce small-scale spectral variance that often results in nonzero parameter values unrelated to true detections. Imposing a minimum value threshold is a useful technique to eliminate or reduce the number of "false-positive" detections.

[43] Some parameter formulations are nonunique in the sense that there is the potential for mineralogic confusion. Care was taken to avoid this whenever possible, but there are a few instances where it is unavoidable. For example, D2400 is formulated to detect hydrated sulfates but also yields positive detections for water ice (see parameter formulations in Table 1 and related reference spectra in Figure 6). Examining correlations between parameters or using filtering processes such as those discussed in section 5.3 can often reduce confusion, but it is important for all critical detections to be verified using the original spectra, or in the case of CRISM, data from subsequent targeting using the full spectral resolution mode.

[44] A similar problem of nonuniqueness is that some of the spectral features tracked with the parameters in Table 1 result from more than one type of mineral. This was discussed above for BD1900; another example is BDI1000, gauging absorption in the 1 μm region. This parameter is designed to detect mafic minerals and ferric oxides but has the potential to detect other materials likely to be present such as dust and glasses, which also have absorptions in this wavelength region even with very little iron [*Erard and Calvin*, 1997; *Nicholis et al.*, 2006]. As was shown above, this situation can be improved upon by assessing the nonunique parameter in concert with other parameters that track more unique spectral features. In addition, this is another situation where minimum value thresholds can be useful. A well chosen threshold value can eliminate all but the strongest signatures, removing values due to weaker signatures associated with minor surface components.

[45] Positive correlations between parameter results and other factors such as albedo or topography can also be misleading. For example, there is a well-documented but not thoroughly understood correlation between albedo and water band depths, such as BD1900 [see *Clark*, 1983; *Milliken and Mustard*, 2005, and references therein]. Another example is the observed tendency for OLINDEX to have larger values in brighter areas, which is often a result of the increase in reflectance in the 1 μm region associated with brighter spectra and not necessarily the presence of olivine. In addition, as mentioned above, some atmospheric parameters display a dependence on altitude, which is correlated to the atmospheric path length. Thus positive correlations between parameter values and albedo or topography may not be directly related to composition and should be fully investigated and corrected for if possible before conclusions are drawn.

21562202e, 2007, E8, Downloaded from https://agupubs.onlinelibrary.wiley.com/doi/10.1029/2006JE002831 by National Health And Medical Research Council, Wiley Online Library on [25/02/2025]. See the Terms and Conditions (https://onlinelibrary.wiley.com/terms-and-conditions) on Wiley Online Library for rules of use; OA articles are governed by the applicable Creative Commons License

[46] Lastly, there are limitations to the interpretations that can be made from spectral parameters.

[47] As discussed in section 2.2, parameter values cannot be easily translated into quantitative abundances, often limiting the conclusions that can be drawn from the data. For continued discussion of this issue, see *Poulet et al.* [2007].

7. Summary

[48] We have examined global, regional, and seasonal examples of products created from multispectral parameters modeled after the summary products that will be created from CRISM data. These multispectral parameters succeed in capturing mineralogic features in spectra from the Martian surface, particularly those related to mafic mineralogy, hydrated silicates and sulfates, and surface ices, as well as features related to known atmospheric constituents. We have shown that spatial grids of these parameters highlight locations with strong mineralogic signatures including all of the regions of interest reported by the OMEGA team, and that seasonal grids support spatial and temporal variations reported by others using the hyperspectral OMEGA data. A brief discussion of caveats and limitations related to the summary products and their interpretation was also presented to assist with their application by the community at large if they are to become a standard CRISM product.

[49] This study demonstrates that the CRISM multispectral data will succeed in capturing the known diversity of the Martian surface and variability of the Martian atmosphere and that, when interpreted with care, the summary products from this data set will be a reliable and useful tool for rapid scientific assessment and targeting support.

[50] **Acknowledgments.** We thank the people responsible for the success of the Mars Express and Mars Reconnaissance Orbiter missions. Thanks go to the OMEGA team for providing the data used in this analysis, particularly Jean-Pierre Bibring and his willingness to collaborate. We also wish to acknowledge Ray Arvidson for his involvement in the development of the CRISM summary products and his useful comments regarding this manuscript and thank Jeffrey Johnson and Michael Abrams for their thoughtful reviews. Spectral lab data used in this work were acquired from the RELAB Spectral Library at Brown University. This research was supported by the Mars Reconnaissance Orbiter Project through NASA contract JHAP852950, and the Mars Critical Data Products Program through JPL contract 1268782.

References

Arvidson, R. E., F. Poulet, J.-P. Bibring, M. Wolff, A. Gendrin, R. V. Morris, J. J. Freeman, Y. Langevin, N. Mangold, and G. Bellucci (2005), Spectral reflectance and morphologic correlations in eastern Terra Meridiani, Mars, *Science*, *307*, 1591–1594.

Bandfield, J. L., V. E. Hamilton, and P. R. Christensen (2000), A global view of Martian surface compositions from MGS-TES, *Science*, *287*, 1626–1630.

Bell, J. F., et al. (2000), Mineralogic and compositional properties of Martian soil and dust: Results from Mars Pathfinder, *J. Geophys. Res.*, *105*, 1721–1755.

Bibring, J.-P., Y. Langevin, A. Soufflot, C. Combes, and C. Cara (1989), Results from the ISM experiment, *Nature*, *341*, 591–593.

Bibring, J.-P., et al. (2004a), Perennial water ice identified in the south polar cap of Mars, *Nature*, *428*, 627–630.

Bibring, J.-P., et al. (2004b), OMEGA: Observatoire pour la Mineralogie, l'Eau, les Glaces et l'Activité, in *Mars Express: The Scientific Payload*, edited by A. Wilson, *Eur. Space Agency Spec. Publ.*, *ESA-SP 1240*, 37–49.

Bibring, J.-P., et al. (2005), Mars surface diversity as revealed by the OMEGA/Mars Express observations, *Science*, *307*, 1576–1581.

Bibring, J.-P., et al. (2006), Global mineralogical and aqueous Mars history derived from OMEGA/Mars Express data, *Science*, *312*, 400–404.

Christensen, P. R., et al. (2001), Mars Global Surveyor Thermal Emission Spectrometer experiment: Investigation description and surface science results, *J. Geophys. Res.*, *106*, 23,823–23,872.

Clancy, R. T., A. W. Grossman, M. J. Wolff, P. B. James, D. J. Rudy, Y. N. Billawala, B. J. Sandor, S. W. Lee, and D. O. Muhleman (1996), Water vapor saturation at low altitudes around aphelion: A key to Mars climate?, *Icarus*, *122*, 36–62.

Clancy, R. T., M. J. Wolff, and P. R. Christensen (2003), Mars aerosol studies with the MGS TES emission phase function observations: Optical depths, particle sizes, and ice cloud types versus latitude and solar longitude, *J. Geophys. Res.*, *108*(E9), 5098, doi:10.1029/2003JE002058.

Clark, R. N. (1983), Spectral properties of mixtures of montmorillonite and dark grains: Implications for remote sensing minerals containing chemically and physically adsorbed water, *J. Geophys. Res.*, *88*, 10,635–10,644.

Clark, R. N. (1999), Spectroscopy of rocks and minerals and principles of spectroscopy, *Remote Sensing for the Earth Sciences*, 3rd ed., vol. 3, edited by A. N. Rencz and R. R. Ryerson, pp. 3–58, John Wiley, New York.

Clark, R. N., and T. L. Roush (1984), Reflectance spectroscopy: Quantitative analysis techniques for remote sensing applications, *J. Geophys. Res.*, *89*, 6329–6340.

Clark, R. N., G. A. Swayze, R. B. Singer, and J. B. Pollack (1990), High-resolution reflectance spectra of Mars in the 2.3-micron region: Evidence for the mineral scapolite, *J. Geophys. Res.*, *95*, 14,463–14,480.

Drossart, P., et al. (2005), Atmospheric Studies with OMEGA/Mars Express, *Proc. Lunar Planet. Sci. Conf. 36th*, Abstract 1737.

Erard, S., and W. Calvin (1997), New composite spectra of Mars, 0.4–5.7 μm, *Icarus*, *130*, 449–460.

Gendrin, A., et al. (2005), Sulfates in Martian layered terrains: The OMEGA/Mars Express view, *Science*, *307*, 1587–1591.

Gendrin, A., et al. (2006), Strong pyroxene absorption bands on Mars identified by OMEGA: Geological counterpart, *Proc. Lunar Planet. Sci. Conf. 37th*, Abstract 1858.

Glotch, T. D., and P. R. Christensen (2005), Geologic and mineralogic mapping of Aram Chaos: Evidence for a water-rich history, *J. Geophys. Res.*, *110*, E09006, doi:10.1029/2004JE002389.

Hamilton, V. E., and P. R. Christensen (2005), Evidence for extensive, olivine-rich bedrock on Mars, *Geology*, *33*, 433–436.

Hapke, B. (1993), *Theory of Reflectance and Emittance Spectroscopy*, Cambridge Univ. Press, Cambridge, U. K.

Hoefen, T. M., R. N. Clark, J. L. Bandfield, M. D. Smith, J. C. Pearl, and P. R. Christensen (2003), Discovery of olivine in the Nili Fossae region of Mars, *Science*, *302*, 627–630.

Jakosky, B. M., and C. B. Farmer (1982), The seasonal and global behavior of water vapor in the Mars atmosphere: Complete global results of the Viking atmospheric water detector experiment, *J. Geophys. Res.*, *87*, 2999–3019.

Johnson, J. R., W. M. Grundy, and M. K. Shepard (2004), Visible/near-infrared spectrogoniometric observations and modeling of dust-coated rocks, *Icarus*, *171*, 546–556.

Jouglet, D., F. Poulet, R. E. Milliken, J. F. Mustard, J.-P. Bibring, Y. Langevin, and B. Gondet (2007), Hydration state of the Martian surface as seen by Mars Express OMEGA: 1. Analysis of the 3 micron hydration feature, *J. Geophys. Res.*, doi:10.1029/2006JE002846, in press.

Kieffer, H. H., and T. N. Titus (2001), TES mapping of Mars' north seasonal cap, *Icarus*, *154*, 162–180.

Kieffer, H. H., T. Z. Martin, S. C. Chase Jr., R. E. Miner, and F. D. Palluconi (1976), Martian north pole summer temperatures—Dirty water ice, *Science*, *194*, 1341–1344.

Langevin, Y., F. Poulet, J.-P. Bibring, B. Schmitt, S. Doute, and B. Gondet (2005a), Summer evolution of the north polar cap of Mars as observed by OMEGA/Mars Express, *Science*, *307*, 1581–1584.

Langevin, Y., F. Poulet, J.-P. Bibring, and B. Gondet (2005b), Sulfates in the north polar region of Mars detected by OMEGA/Mars Express, *Science*, *307*, 1584–1586.

Maltagliati, L., D. Titov, H. U. Keller, M. Garcia-Comas, and J.-P. Bibring (2006), Water vapor retrieval in the atmosphere of Mars: Results from the OMEGA experiment onboard Mars Express, paper presented at Second Workshop on Mars Atmosphere Modelling and Observations, Cent. Natl. d'Etudes Spatiales, Granada, Spain.

McGuire, P. C., M. J. Wolff, R. E. Arvidson, M. D. Smith, R. T. Clancy, S. L. Murchie, J. F. Mustard, S. M. Pelkey, and T. Z. Martin (2006), Retrieval of surface Lambert albedos from the Mars Reconnaissance Orbiter CRISM data, *Proc. Lunar Planet. Sci. Conf. 37th*, Abstract 1529.

Milliken, R. E., and J. F. Mustard (2005), Quantifying absolute water content of minerals using near-infrared reflectance spectroscopy, *J. Geophys. Res.*, *110*, E12001, doi:10.1029/2005JE002534.

21562202e, 2007, E8, Downloaded from https://agupubs.onlinelibrary.wiley.com/doi/10.1029/2006JE002831 by National Health And Medical Research Council, Wiley Online Library on [25/02/2025]. See the Terms and Conditions (https://onlinelibrary.wiley.com/terms-and-conditions) on Wiley Online Library for rules of use; OA articles are governed by the applicable Creative Commons License

Murchie, S., L. Kirkland, S. Erard, J. Mustard, and M. Robinson (2000), Near-infrared spectral variations of Martian surface materials from ISM imaging spectrometer data, *Icarus*, *147*, 444–471.

Murchie, S., et al. (2007), Compact Reconnaissance Imaging Spectrometer for Mars (CRISM) on Mars Reconnaissance Orbiter (MRO), *J. Geophys. Res.*, *112*, E05S03, doi:10.1029/2006JE002682.

Mustard, J. F., and J. M. Sunshine (1999), Spectral analysis for earth science investigation, in *Remote Sensing for the Earth Sciences*, 3rd ed., vol. 3, edited by A. N. Rencz, and R. R. Ryerson, pp. 3–58, John Wiley, New York.

Mustard, J. F., S. Murchie, S. Erard, and J. Sunshine (1997), In situ compositions of Martian volcanics: Implications for the mantle, *J. Geophys. Res.*, *102*, 25,605–25,616.

Mustard, J. F., F. Poulet, A. Gendrin, J.-P. Bibring, Y. Langevin, B. Gondet, N. Mangold, G. Bellucci, and F. Altieri (2005), Olivine and pyroxene diversity in the crust of Mars, *Science*, *307*, 1594–1597.

Nicholis, M., R. E. Milliken, J. F. Mustard, and M. Rutherford (2006), VIS-NIR Spectral Properties of Olivine in a Basaltic Glass: Implications for Olivine-rich Terrains on Mars, *Proc. Lunar Planet. Sci. Conf. 37th*, Abstract 2378.

Pieters, C. M. (1983), Strength of mineral absorption features in the transmitted component of near-infrared reflected light: First results from RELAB, *J. Geophys. Res.*, *88*, 9534–9544.

Poulet, F., J.-P. Bibring, J. F. Mustard, A. Gendrin, N. Mangold, Y. Langevin, R. E. Arvidson, B. Gondet, C. Gomez, and the Omega Team (2005), Phyllosilicates on Mars and implications for early Martian climate, *Nature*, *438*, 623–627.

Poulet, F., C. Gomez, J.-P. Bibring, Y. Langevin, B. Gondet, G. Belluci, J. Mustard, and the Omega Team (2007), Martian surface mineralogy from OMEGA/Mars Express: Global mineral maps, *J. Geophys. Res.*, doi:10.1029/2006JE002840, in press.

Schmitt, B., S. Doute, Y. Langevin, F. Forget, J. Bibring, G. Bellucci, F. Altieri, F. Poulet, and B. Gondet (2005), Spring sublimation of the seasonal condensates on Mars from OMEGA/Mars Express, *Eos Trans. AGU*, *86*(52), Fall Meet. Suppl, Abstract P23C-02.

Smith, M. D. (2002), The annual cycle of water vapor on Mars as observed by the Thermal Emission Spectrometer, *J. Geophys. Res.*, *107*(E11), 5115, doi:10.1029/2001JE001522.

Sprague, A. L., D. M. Hunten, L. R. Doose, and R. E. Hill (2003), Mars atmospheric water vapor abundance: 1996–1997, *Icarus*, *163*, 88–101.

Sunshine, J. M., C. M. Pieters, and S. F. Pratt (1990), Deconvolution of mineral absorption bands: An improved approach, *J. Geophys. Res.*, *95*, 6955–6966.

Thomas, P. C., M. C. Malin, K. S. Edgett, M. H. Carr, W. K. Hartmann, A. P. Ingersoll, P. B. James, L. A. Solderblom, J. Veverka, and R. Sullivan (2000), North-south geological differences between the residual polar caps on Mars, *Nature*, *404*, 161–164.

Zasova, L. V., et al. (2006), Ozone in Martian atmosphere from the 1.27 μm O_2 emission: OMEGA/Mars Express measurements, paper presented at Second Workshop on Mars Atmosphere Modelling and Observations, Cent. Natl. d'Etudes Spatiales, Granada, Spain.

J.-P. Bibring, B. Gondet, Y. Langevin, and F. Poulet, Institut d'Astrophysique Spatiale, Bâtiment 121, F-91405 Orsay Campus, France.

R. T. Clancy and M. Wolff, Space Science Institute, 4750 Walnut Street, Suite 205, Boulder, CO 80301, USA.

A. Gendrin, R. Milliken, J. F. Mustard, and S. M. Pelkey, Department of Geological Sciences, Brown University, Box 1846, Providence, RI 02912-1846, USA. (shannon_pelkey@brown.edu)

S. Murchie, Applied Physics Laboratory, Laurel, MD 20723, USA.

M. Smith, NASA Goddard Space Flight Center, Mail Code 693, Greenbelt, MD 20771, USA.

21562202e, 2007, E8, Downloaded from https://agupubs.onlinelibrary.wiley.com/doi/10.1029/2006JE002831 by National Health And Medical Research Council, Wiley Online Library on [25/02/2025]. See the Terms and Conditions (https://onlinelibrary.wiley.com/terms-and-conditions) on Wiley Online Library for rules of use; OA articles are governed by the applicable Creative Commons License